THERMAL NONLINEARITY IN RADIO FREQUENCY PIEZOELECTRIC LATERALLY VIBRATING RESONATORS

BY

RUOCHEN LU

THESIS

Submitted in partial fulfillment of the requirements
for the degree of Master of Science in Electrical and Computer Engineering
in the Graduate College of the
University of Illinois at Urbana-Champaign, 2017

Urbana, Illinois

Adviser:

Assistant Professor Songbin Gong

Abstract

In recent years, the demand for more wireless bandwidth (BW) has been soaring due to the booming of wireless applications in the marketplace and customers' pursuit of higher data rates for communication. This need for more BW will continue to grow as the Internet of Things (IoT) foreshadows more applications requiring wireless connectivity and the use of radio spectrum. As a result, radio frequency (RF) front-end platforms capable of meeting the stringent requirements of higher performance and wider bandwidth are highly sought after and currently being heavily researched. These new platforms should be capable of dynamically operating in several dozens of frequency bands while maintaining high performance.

RF piezoelectric laterally vibrating resonators (LVRs) have recently emerged as a promising candidate for front-end filtering and multiplexing in future radios. Compared with the incumbent filtering technology, such as thin-film bulk acoustic resonators (FBARs) and surface acoustic wave resonators (SAWs), this new class of microelectromechanical systems (MEMS) features an assortment of advantages, including integration capability with CMOS, frequency scalability towards higher frequencies, greater electromechanical coupling, and lower loss. Despite these promising features, LVRs still face the challenge of attaining linear response at high power levels and diminishing the intermodulation distortion. The moderate linearity and power handling, which are caused by the intrinsic thermal nonlinearity, produce an unacceptable amount of interference in front-ends. In this thesis, an analytical method has been developed to predict the thermal nonlinearity accurately. It is subsequently leveraged to reduce the nonlinear behavior of LVRs.

The organization of the thesis is as follows. In Chapter 1, fundamentals of MEMS resonators are discussed. Chapter 2 explains the operating principles of piezoelectric LVRs in detail, describes the dominant nonlinearities in piezoelectric LVRs, and presents the prior studies on nonlinearities in piezoelectric LVRs. In Chapter 3, a quantitative approach is presented to precisely model the nonlinear dynamics and accurately predict the intermodulation distortions in LVRs. Chapter 4 focuses on the experimental validation of the theoretical analysis. The last chapter concludes with the impact of the method described herein on guiding future optimizations and enhancing the power handling of LVRs for real-world applications.

Acknowledgments

First of all, I want to express my gratitude to my MS adviser, Prof. Songbin Gong, for giving me the opportunity to join the Illinois Integrated RF Microsystems Group (ILIRM) at UIUC. This work would not have been finished without his full support. With his encouragement and advice, Prof. Gong had led me into an exciting adventure of scientific and engineering inquiries.

Second, I would like to give special thanks to the enthusiastic individuals in the ILIRM group. I have been very fortunate to receive advice from with Dr. Yong-Ha Song, Dr. Tomas Manzaneque, and Dr. Daotong Li. The many productive discussions I had with them have inspired me to pursue new approaches and solutions that would otherwise be missed. In addition, I am truly thankful for my labmates, Anming Gao, Yansong Yang, Michael G. Breen, Brandon Arakawa, Arunita Kar, John Krol, Ali Kourani, and Sarah Shim. They have fostered a great atmosphere filled with comradery and friendship, allowing me to accomplish my academic goals while feeling the sense of belonging.

Third, I want to acknowledge the academic collaboration with Prof. Daniel Wasserman, Runyu Liu of UIUC, Mattan Kamon, and Rahul Jhaveri of Coventor Inc. They have broadened my research horizon and introduced new research fields to me. The intriguing teamwork will be one of my best memories.

Fourth, my thanks go to my friends Zelei Sun, Yuheng Bu, Weihao Gao, Du Su, Sitao Huang, and Ou Liang for giving me many moments that I will never forget.

Finally, I must give my most sincere thanks to my family, who have supported me unconditionally and shaped my existence as a scholar, friend, and son.

Table of Contents

Chapter 1 Introduction

In this chapter, the background and the motivation of MEMS are first introduced. Among various MEMS applications, RF MEMS resonators are chosen to be the primary focus of this thesis. Next, MEMS resonators are categorized based on mechanical modes and transduction mechanisms. Features of different types of MEMS resonators are discussed. To better understand MEMS resonators, a linear model for the devices is presented. Finally, for more sophisticated situations where resonators are operating in nonlinear regime, the fundamentals of nonlinear MEMS resonator models are reviewed.

1.1 MEMS Technology

In the past few decades, the development of microfabrication techniques has enabled complex micrometer-scale machines, giving birth to a discipline called microengineering [1]. A wide range of microscale devices leveraging coupled physics between multiple domains (e.g. mechanics, optics, electromagnetism, fluid dynamics, etc.), particularly the electrical and mechanical domains, has emerged and enabled numerous new applications in actuators, sensors, and signal processing. These devices are called MEMS [2]. The pioneering work [3] in the early 1980s featured the possibility of scaling down devices with different goals using well-developed semiconductor fabrication techniques.

The fabrication process of MEMS devices usually consists of a sequence of lithographical patterning, deposition, and etching. The patterning is usually defined by photolithography, transferring the geometric patterns from a photomask to a light-sensitive photoresist on the substrate [4]. The deposition of thin films and materials includes electroplating, chemical vapor deposition, plasma-enhanced chemical vapor deposition, evaporation, sputtering, etc. The etching process can be divided into two categories, the surface micromachining [5] and bulk micromachining [6]. The surface micromachining involves creating suspended structures with a sacrificial layer, while the bulk micromachining typically involves the etching of a thickness comparable to wafer for creating cavities.

MEMS technology is an efficient energy transduction conduit between the electrical and mechanical domains, thus allowing systems to harness many desirable features of the mechanical domain for processing electrical signals. Many applications that exploit the cross-domain nature of MEMS devices can be found in the literature, such as energy harvesters [7], optical switches [8], RF switches [9], RF resonators [10], ink injection [11], atomic force microscopy (AFM) [12], pressure sensors [13], microphones[14], and accelerometers [15]. This thesis primarily focuses on RF MEMS resonators.

1.2 MEMS Resonators

A MEMS resonator is a microelectromechanical device that is engineered to have a specific resonant frequency for applications such as timing, filtering, and sensing. Motivated by overcoming the shortcomings of quartz crystal resonators, resonance properties of microstructures have been studied since the 1960s [16]. Advancements of material, microfabrication techniques, and novel designs have fueled the development of MEMS resonators. Nowadays, the high frequency mechanical filters are irreplaceable due to their high performance (i.e. higher *Q*) and compact size [17].

Table 1.1 Classification of MEMS resonators based on the mode of vibration.

Mode of Vibration	Frequency Range	Example
Flexural	10 kHz – 10 MHz	[18]
Contour	10 MHz – 10 GHz	[10]
Thickness Extensional	500 MHz – 20 GHz	[19]
Shear	800 MHz -2 GHz	[20]

As seen in Table 1.1, a variety of MEMS resonators (Fig. 1.1), classified based on the mode of vibration, are developed. Flexural mode resonators typically have resonances at low frequencies and are suitable for high *Q* and low frequency oscillator applications. Contour mode or Lamb wave resonators have their resonant frequencies set primarily by lithographic processes [i.e. the lateral (in-plane) dimensions of the structure]. Thickness extensional mode devices are known as thin-film bulk acoustic resonators (FBARs), and are the commercial solution for filtering in RF front ends. Shear mode devices have a high stiffness and can operate at high frequencies. Without a net

volume change, this mode theoretically yields high mechanical *Q* (low damping) and low temperature sensitivity [21].

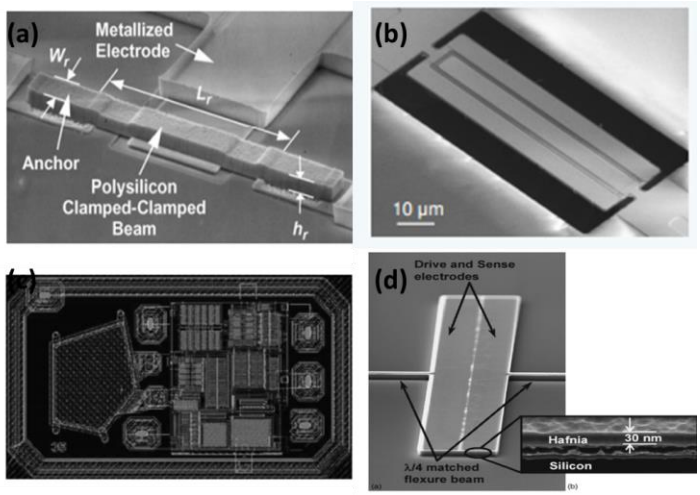

Figure 1.1 MEMS resonators with various modes of vibration. (a) Flexural mode device [18]. (b) Contour mode device [22]. (c) Thickness extensional mode device [23]. (d) Shear mode device [20].

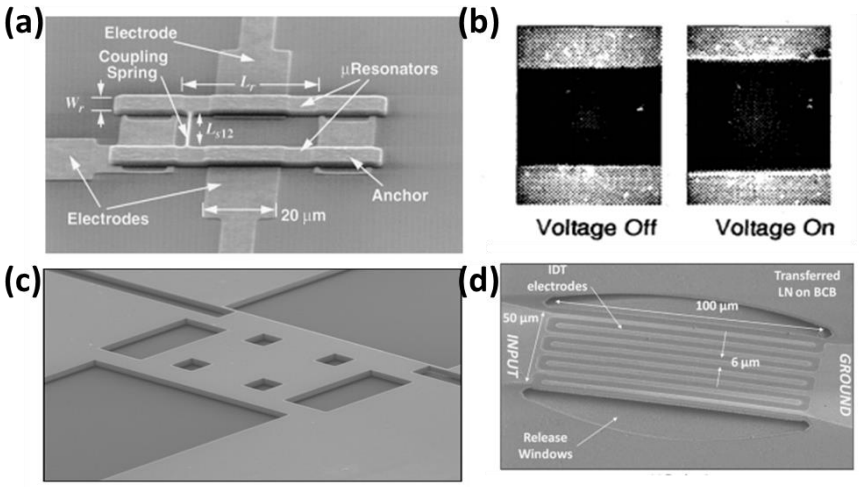

Figure 1.2 MEMS resonators with various transduction mechanisms. (a) Electrostatics [18]. (b) Electrostriction [24]. (c) Thermoelasticity effect [25]. (d) Piezoelectricity effect [26].

MEMS resonators can also be categorized according to their electromechanical transduction mechanisms, such as electrostatics [18], electrostriction [24], thermoelasticity [25], and piezoelectricity [26] (Fig. 1.2). The advantages of each mechanism are listed in Table 1.2. In this thesis, the piezoelectric contour mode resonators (more generally LVRs) will be the focus for several reasons. First, piezoelectric actuation has a high-energy transduction efficiency at RF than

other actuation mechanism. Second, the state of the art piezoelectric materials (e.g. AlN and $LiNbO_3$) have been demonstrated with low acoustic loss and high *Q*. Third, the resonance of a LVR is mainly determined by the lateral dimensions, thus enabling great frequency salability by lithography and monolithically integration of devices with multiple center frequencies.

Table 1.2 Classification of MEMS resonators based on transduction mechanism.

Mode of Vibration	Advantages	Example
Electrostatics	High *Q*	[18]
Electrostriction	Highest *f*-*Q* product in MEMS resonator	[24]
Thermoelasticity	Scales advantageously to higher frequencies	[25]
Piezoelectricity	Piezoelectric coupling is strong, commercial success	[26]

1.3 Modeling of MEMS Resonators

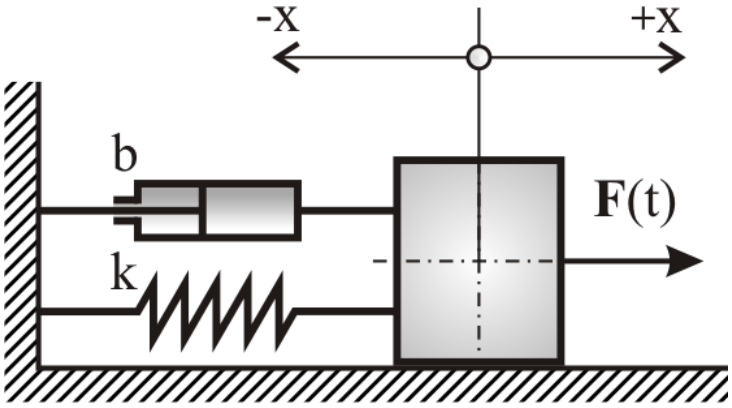

Figure 1.3 Linear second-order single-degree-of-freedom (SDOF) system[27].

To model the mechanical response of a MEMS resonator, regardless of its actuation mechanism, a single-degree-of-freedom (SDOF) system is first discussed for simplicity (Fig. 1.3). Assume that a mass *m* is moved along the x-axis under the influence of 3 forces: a restoring force from a spring with a spring constant of *k*, a damping proportional to the velocity by constant *b* and an external force *F(t)*. The second-order differential equation for the displacement *u(t)* can be represented as [28] :

$$m\frac{d^2u(t)}{dt^2} + b\frac{du(t)}{dt} + ku(t) = F(t) \tag{1.1}$$

$$\ddot{u(t)} + 2\zeta\omega_n \dot{u(t)} + \omega_n^2 u(t) = \frac{F(t)}{m} \tag{1.2}$$

where the natural resonance of the system ω_n and the damping ratio ζ are defined as [28] :

$$\omega_n = \sqrt{\frac{k}{m}} \tag{1.3}$$

$$\zeta = \frac{b}{2m\omega_n} \tag{1.4}$$

Under the free vibration condition where *F(t)* is absent, the solution can be presented for an underdamped system as [28] :

$$u(t) = u_0 e^{-\zeta\omega_n t}\cos(\omega_n\sqrt{1-\zeta^2}t - \theta_0) \tag{1.5}$$

where u_o and θ_0 are dependent on the initial conditions of the system. The quality factor *Q* is defined as 2π times the energy stored in the system divided by the energy dissipated per cycle, which can also be rewritten as [28] :

$$Q = \frac{1}{2\zeta} \tag{1.6}$$

As presented in Eq. 1.5, the *Q* also can be defined as the number of cycles needed to reduce the by a factor of $e^{2\pi}$.

For an n-degree-of-freedom (n-DOF) system, the behavior of the system can be described by Eq. 1.1, with *m*, *b*, *k* becoming n^{th}-order symmetrical matrices. The model essentially presents an eigenvalue problem. It can be proven that the eigenvectors of a n-DOF problem can form a set of orthogonal bases [28]. Hence, the displacement of the bodies comprising the system can be expressed as a linear superposition of the eigenvectors or vibration modes.

For a more sophisticated model considering all the physics parameters as distributed cases, based on Eq. 1.1, the finite element method (FEM) can be used to achieve more accurate prediction of the mechanical resonance [21].

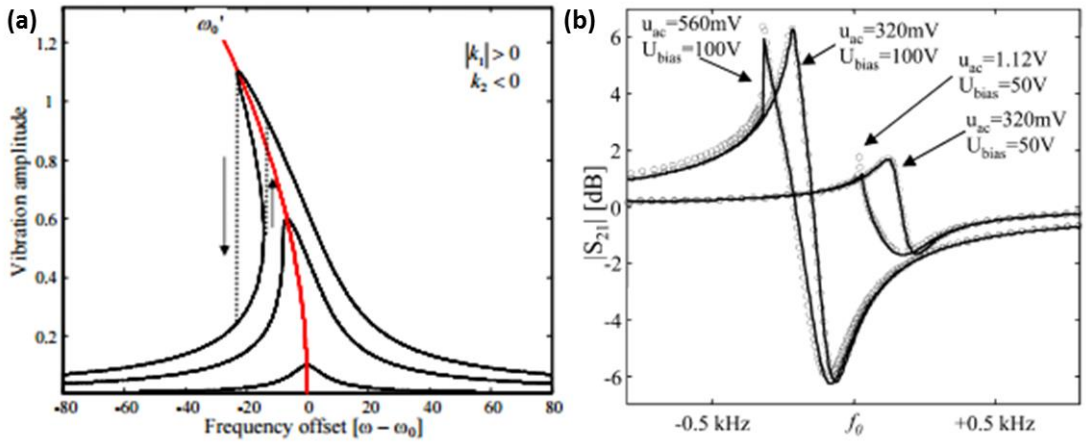

Figure 1.4 Typical solutions of a Duffing equation model.(a) Calculated vibration amplitude in a system with nonlinear elasticity [29]. (b) Measured nonlinear response of an electrostatic resonator [30].

1.4 Nonlinearity in MEMS Resonators

Typically, a MEMS resonator is modeled and considered as a linear system, in which the force is only linearly related to the displacement. However, a MEMS resonator can be driven into the nonlinear regime for a number of different reasons [31]. Despite their different physical origins, the nonlinear response in a MEMS resonator can be studied with a simplified model that includes a nonlinear elastic term in Eq. 1.1, as [30]:

$$m\frac{d^2u(t)}{dt^2} + b\frac{du(t)}{dt} + k_1u(t) + k_3u(t)^3 = F(t) \tag{1.7}$$

Such an equation is referenced as the Duffing equation [32]. The solution of the equation can be analytically approximated or numerically attained. Using an analytical approximation, the resonant frequency can be expressed as [30]:

$$\omega_n' = \omega_n + \frac{3k_3}{8k_1}\omega_n X_0 \tag{1.8}$$

where X_0 is related to the boundary conditions. A typical solution and measured response for an electrostatic MEMS resonator are shown in Fig. 1.4.

The solutions of the nonlinearity imply that more linear transduction and resonant modes should be leveraged to minimize the nonlinearity. Piezoelectric transduction and bulk modes are ideal for

such requirements [33]. However, for applications leveraging the nonlinear effects, electrostatic transduction and flexural modes are more suitable [34].

Chapter 2 Piezoelectric MEMS LVRs and Their Nonlinearities

As discussed in the last chapter, this thesis focuses on piezoelectric MEMS resonators due to their high-energy transduction efficiency and other merits. To appreciate the high electromechanical coupling found in piezoelectric MEMS resonators, the fundamentals of piezoelectricity are first discussed in this chapter. The designs, fabrication, and performance of piezoelectric MEMS LVRs are then introduced, followed by the discussions on the nonlinearities in piezoelectric MEMS LVRs. Last, previous studies on reducing or harnessing nonlinearities in piezoelectric resonators are presented.

2.1 Fundamentals of Piezoelectricity

The piezoelectric effect is the capacity of certain materials to interchange energy between the mechanical and electrical domains [35]. The direct effect transforms a force applied to the material into internal electrical charges, while the reverse effect leads to the generation of mechanical strain through the application of an electric field. Typical piezoelectric materials include piezoelectric crystals, piezoelectric ceramics and polymers [36]. Only materials of which the lattice structures lack a center of symmetry can possess piezoelectricity as shown in Fig. 2.1. The electric moment generated by the elastic deformation is the origin of piezoelectricity. Other crystals due to their centrosymmetry (e.g. Si), do not exhibit piezoelectricity.

The piezoelectricity is usually a linear process, and its constitutive relationships are expressed as [36]:

$$D = \varepsilon^T E + dT \tag{2.1}$$

$$S = d_t E + s^E T \tag{2.2}$$

where T is the stress, S is the strain, E is the electric filed strength, D is the electric displacement, ε^T is permittivity with constant stress, s^E is the elastic compliance with constant electric field strength, d is the piezoelectric strain constant with the subscript t referring to the transposed matrix. The units of the parameters are shown in Table 2.1. Due to the reciprocity in the definitions of S and T, d is a 6 by 3 matrix, S, T are 1 by 6 matrices, and s is a 6 by 6 matrix [37].

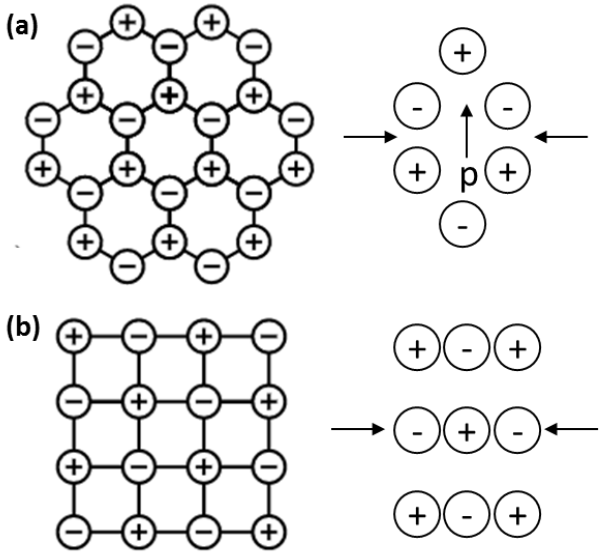

Figure 2.1 Electric moment generation in crystals under elastic deformation. (a) A hexagon cell with piezoelectricity. (b) A square cell without piezoelectricity.

Table 2.1 Symbols and units for piezoelectric constants.

Parameter	Symbol	Unit	Parameter	Symbol	Unit
Stress	T	N/m^2	Elastic compliance	s	m^2/N
Strain	S	m/m	Elastic stiffness	c	N/m^2
Electric field strength	E	V/m	Permittivity	ε	F/m
Electric displacement	D	C/m^2	Piezoelectric strain constant	d	C/N

The piezoelectricity can be characterized by dimensionless constants to present the strength of the electromechanical effect. A piezoelectric coupling factor (K) is defined as the square root of the ratio of energy available in the electric form to total input mechanical energy or that of energy available in the mechanical domain to the total input electric energy. Such a coupling factor depends on the electric and mechanical boundary conditions [36]. For a fundamental longitudinal resonant mode excited by a transverse electric field (LE_t mode), K is defined as [36]:

$$K = d_{31}/\sqrt{s_{11}^E \varepsilon_{33}^T} \tag{2.3}$$

where the piezoelectric constant d_{31} describes interaction between the electric field in out-of-plane direction and in-plane extensional strain, s_{11}^E is the in-plane elastic compliance and ε_{33}^T is the

permittivity in polar direction. K^2 sets the ultimate energy transduction efficiency with a given material and given boundary conditions. However, the transducer effective coupling factor, which is more commonly used in evaluating device performance, depends on both the K^2 and transducer design. For a transducer embedded in a resonant element, the effective coupling factor (k_{eff}) can be evaluated with [36]:

$$k_{eff}^2 = \frac{f_p^2 - f_s^2}{f_p^2} \tag{2.4}$$

where f_s and f_p are defined as the series and parallel resonances. For lateral modes, considering that the overtones of the fundamental modes form an exact odd harmonic sequence, we have effective electromechanical coupling factor (k_t) for lateral modes defined as [36]:

$$k_t^2 = k_{eff}^2 \left(1 + \frac{1}{9} + \frac{1}{25} + \cdots\right) = \frac{\pi^2}{8} k_{eff}^2 \tag{2.5}$$

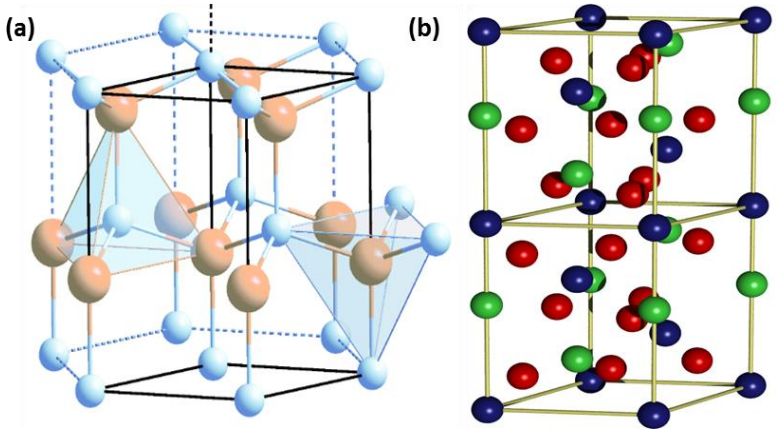

Figure 2.2 Lattice structure of piezoelectric crystals. (a) AlN [38]. (b) $LiNbO_3$ [39].

This thesis focuses on two piezoelectric materials, namely AlN and $LiNbO_3$ (Fig. 2.2). AlN is a well-known piezoelectric material that has reasonably high piezoelectric constants and integration capability with CMOS [40]. AlN thin films can typically be deposited using reactive sputtering processes where an Al target is sputtered in a N_2 filled chamber. Even though the sputtered AlN thin films are polycrystalline, radio frequency acoustic waves exhibit low propagation loss in them. Most lateral modes also have high phase velocities in AlN, and thus support good frequency scalability.

In contrast, $LiNbO_3$ is also a known piezoelectric material but with even higher electromechanical coupling coefficients. Despite its pronounced piezoelectricity, it was not until recently that thin film $LiNbO_3$ became available thanks to the techniques of ion slicing and film transfer. Consequently, lateral extensional mode [26] and shear mode [41] induced by lateral electrical fields have been demonstrated to achieve piezoelectric resonators with high figures of merit (FOM)[26].

2.2 Piezoelectric MEMS LVRs

Piezoelectric resonators operating in a variety of modes have been demonstrated [10], [42]. Among different resonant modes, as discussed in Chapter 1.2, LVRs have various advantages including their high Q, high k_t^2 and potential for monolithically integrating resonators of different resonances. Therefore, piezoelectric LVRs have been vastly researched in the past decade and are chosen to be the focus of this thesis. Design, modeling, fabrication and applications of LVRs will be introduced consequently in this section.

2.2.1 Design and Modeling of Piezoelectric LVRs

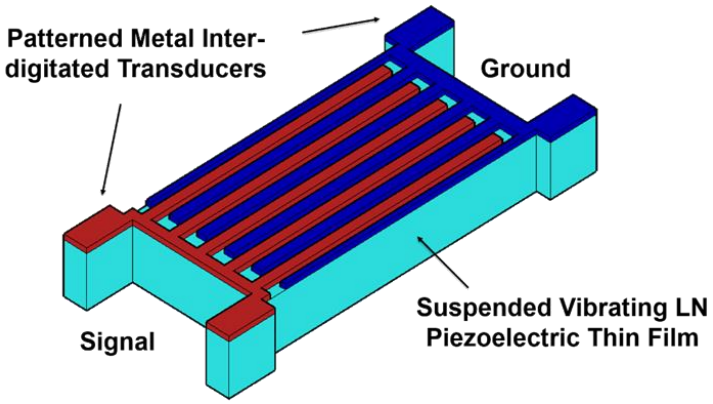

Figure 2.3 Mocked-up view of a typical LVR.

As shown in Fig. 2.3, a typical piezoelectric LVR is composed of a suspended piezoelectric thin film and patterned interdigitated transducers (IDTs). The configuration of the IDTs varies depending on the piezoelectric material in use, and whether a one-port or two-port device is being constructed. More detailed discussions can be found in [43]. For instance, in a one-port $LiNbO_3$ device, the IDTs are alternatingly connected to the ground and signal to generate lateral electric

fields in the resonator body and excite the device into lateral extensional mode vibration via the d_{31} piezoelectric coefficient of AlN. Acoustic standing waves are subsequently formed in the lateral direction off the reflective acoustic boundaries. In a similar fashion with only top electrodes, $LiNbO_3$ based LVRs can be excited with lateral E-fields to accommodate the acoustic standing waves (Fig. 2.4). It is noteworthy that to satisfy the boundary condition of the mechanical resonance for a maximum k_t^2, a weighted electrode technique is typically adopted in $LiNbO_3$ LVRs [44].

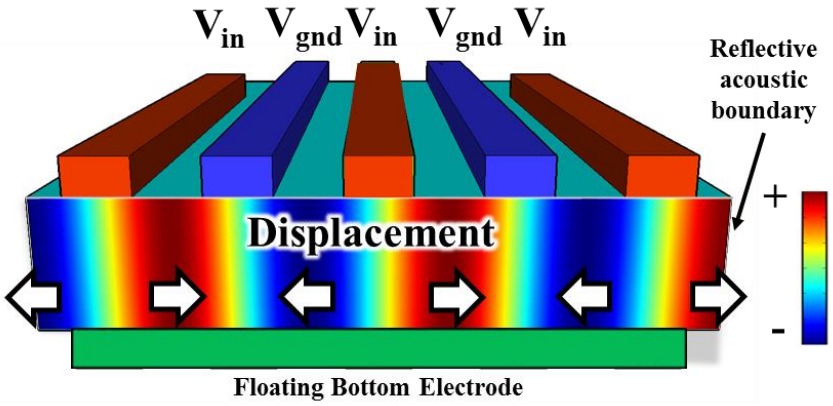

Figure 2.4 Electrical field and piezoelectric effect in the resonator.

The resonant frequency is collectively determined by the lateral dimensions and material properties. The resonant frequency can be approximated as [10]:

$$\omega_s = \frac{\pi}{W_e}\sqrt{\frac{E_{eq}}{\rho_{eq}}} \tag{2.6}$$

where ω_s is the resonance frequency, W_e is the width of pitch, E_{eq} and ρ_{eq} are the equivalent Young's modulus and density of the film stack forming the resonator respectively.

For operations in the linear regime, the electromechanical behavior can be described by the modified Butterworth–Van Dyke (MBVD) model (Fig. 2.5) to represent the mechanical resonance in the electrical domain, described as [10]:

$$R_m = \frac{\pi^2}{8}\cdot\frac{1}{\omega_s^2\cdot C_0}\cdot\frac{1}{k_t^2 Q} \tag{2.7}$$

$$C_m = \frac{8}{\pi^2} \cdot C_0 k_t^2 \tag{2.8}$$

$$L_m = \frac{\pi^2}{8} \cdot \frac{1}{\omega_s^2 \cdot C_0} \cdot \frac{1}{k_t^2} \tag{2.9}$$

$$Z = \frac{1}{j\omega C_0} // (R_m + j\omega L_m + \frac{1}{j\omega C_m}) \tag{2.10}$$

The symbols are explained in Table 2.2. The motional terms represent the mechanical vibration as electrical components. In addition to the current generated by the modal response of the structure, the dielectric behavior of the piezoelectric layer must be taken into account through the inclusion of a static capacitance C_o in parallel.

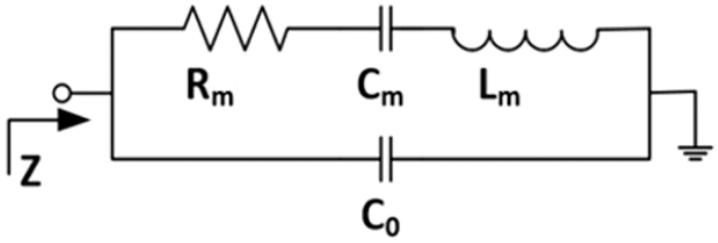

Figure 2.5 MBVD model for piezoelectric resonators.

Table 2.2 Parameters in the MBVD model.

Symbol	Parameter	Unit	Symbol	Parameter	Unit
ω_s	Resonant Frequency	rad/s	k_t^2	Electromechanical Coupling Coefficient	1
Q	Quality Factor	1	C_0	Static Capacitance	F
R_m	Motional Resistance	Ω	C_m	Motional Capacitance	Ω
L_m	Motional Inductance	H	Z	Impedance	Ω

2.2.2 Fabrication of Piezoelectric LVRs

The fabrication of LVRs has been extensively investigated in the past decade [10]. The devices used as the testbed for the investigation in this thesis were fabricated using processes shown in Fig. 2.6.

On the one hand, for AlN LVRs, a four-mask, CMOS compatible process is adopted on a 4-inch high resistivity Si wafer. First, 80 nm of Pt is evaporated as bottom electrode. Then, 500 nm AlN is reactively sputtered. Phosphoric acid is used to etch the ground vias. Then the Al is sputtered to

form the top electrodes. Inductively coupled plasma reactive-ion etching (ICP-RIE) is utilized to define the resonator boundaries and open the release windows. For the last step, the device is released by XeF_2 based etching of Si. The scanning electron microscope (SEM) image of a fabricated device is presented in Fig. 2.7(a).

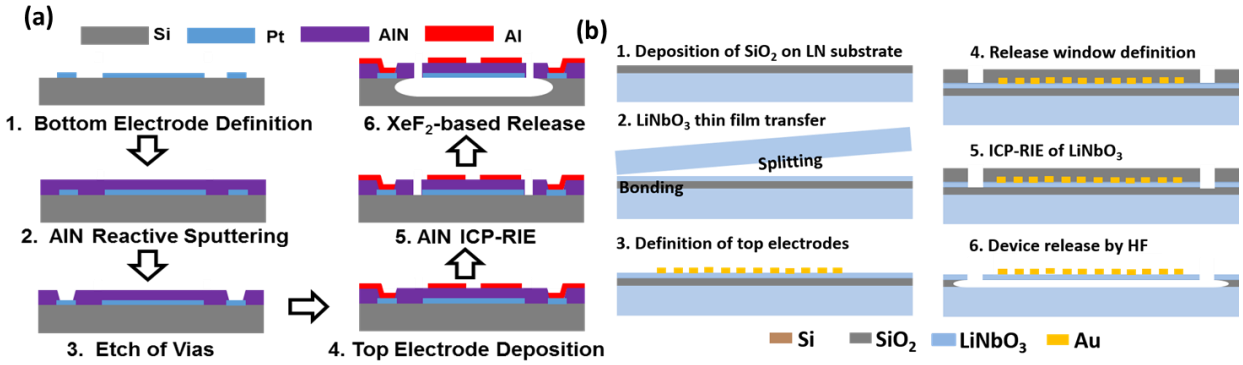

Figure 2.6 Fabrication flow chart of piezoelectric LVRs. (a) AlN LVR. (b) $LiNbO_3$ LVR.

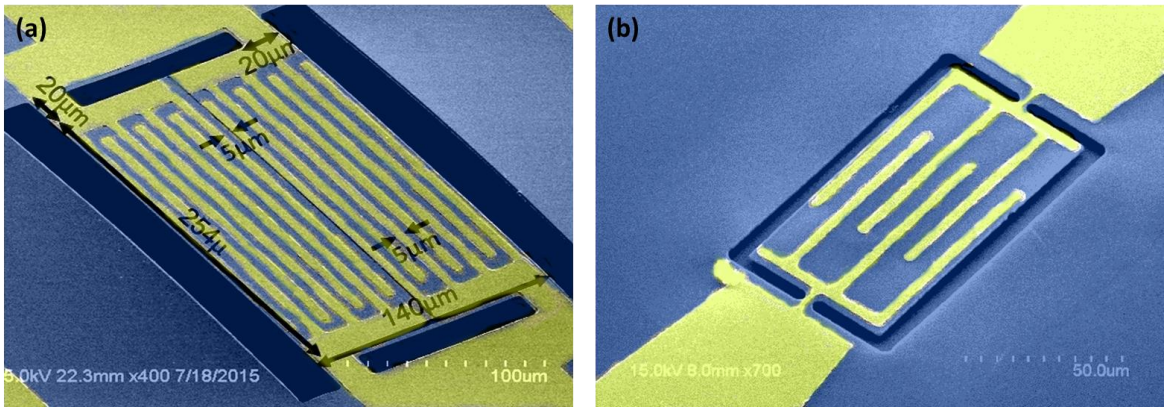

Figure 2.7 SEM of the fabricated piezoelectric LVRs. (a) AlN LVR [43]. (b) $LiNbO_3$ LVR [44].

On the other hand, $LiNbO_3$ LVRs are fabricated with a different method [45], [46], as seen in Fig. 2.6(b). A $LiNbO_3$ thin film on a carrier substrate with an intermediate SiO_2 layer are first fabricated by the vendor NanoLN (Jinan, China). Next, gold electrodes are defined on the top of the thin film. Then, SiO_2 layer is used as the hard mask and $LiNbO_3$ is etched by ICP-RIE for defining the release windows and reflective boundaries. Last, SiO_2 is removed by HF and the resonator is released. The SEM of a fabricated $LiNbO_3$ resonator is shown in Fig. 2.7.

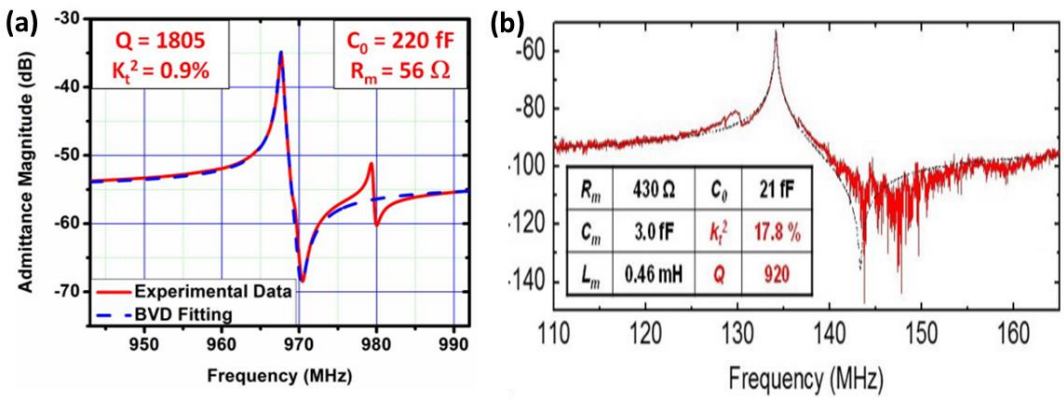

Figure 2.8 Typical LVR admittance responses. (a) Typical AlN resonator [47]. (b) Typical $LiNbO_3$ resonator [48]. The extracted parameters of the MBVD model are shown in the inset tables.

Table 2.3 Reported performance of piezoelectric LVRs.

Reference	Material	k_t^2	*Q*	Frequency
[10]	AlN	1.2%	2100	86 MHz
[49]	AlN	0.3%	414	8.5 GHz
[50]	GaN	0.83%	1174	163 MHz
[48]	$LiNbO_3$	17.8%	920	132 MHz
[51]	$LiNbO_3$	17.5%	1400	460 MHz

2.2.3 Performances and Applications of Piezoelectric LVRs

Typical performances of one-port piezoelectric LVRs, shown in admittance, are presented in Fig. 2.8. Reported performance of piezoelectric resonators is shown in Table 2.3 for AlN [10], [49], GaN [50], and $LiNbO_3$ [48], [51] resonators. Various approaches are used to optimize different performance aspects of LVRs (e.g. spurious mode suppression [41], [52], and quality factor improvement [53]).

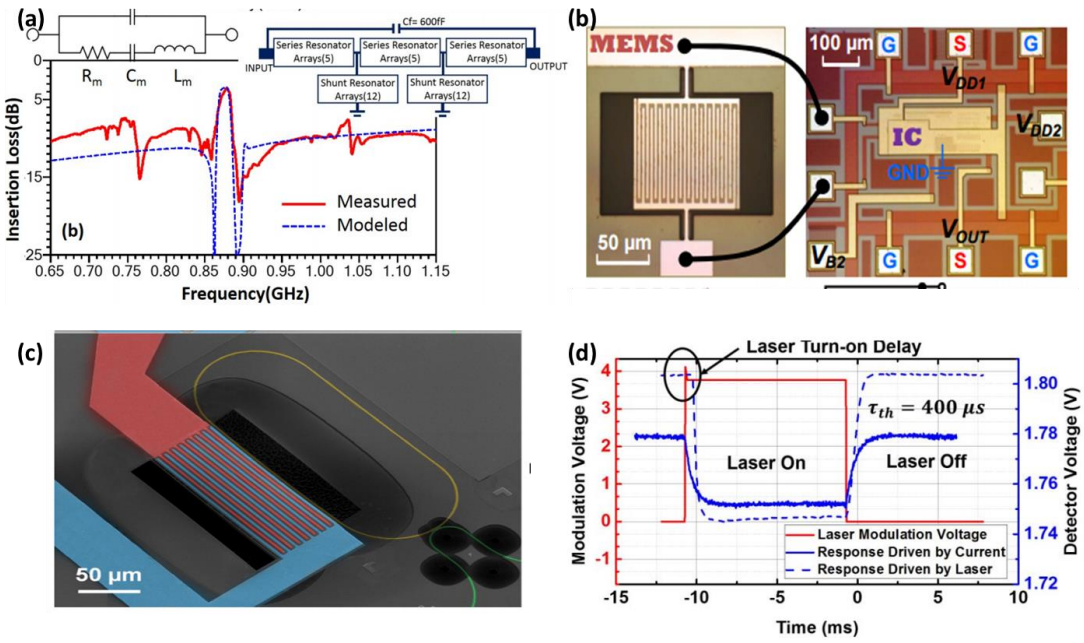

Figure 2.9 Typical LVR applications. (a) RF filtering font-end [54]. (b) Integrated oscillator [55]. (c) Optical modulation [56]. (d) Sensors [57].

A number of applications as seen in Fig. 2.9 have been proposed based on piezoelectric LVRs. Leveraging the low loss and high electromechanical coupling of piezoelectric LVRs, high performance filters [54] have been demonstrated with great potential for future monolithic multi-frequency wideband RF filters. Integrated oscillators [55] have also been demonstrated, providing an alternative method for miniature timing. Using the mechanical vibrations of the LVRs to acousto-optically affect the coupling of light, optical modulators have been shown [56]. Sensors [57], [58], [59] with high sensitivity and small sizes are reported for a wide range of purposes.

Although the LVRs have been demonstrated with promising applications in RF, one major challenge, namely the inherent nonlinearity in miniature piezoelectric LVRs at high power levels, remains a bottleneck in the path of their deployment in RF front ends. The nonlinearity in LVRs performance leads to undesirable performance degradation of their comprising RF systems (e.g. higher insertion loss and intermodulation for filters, larger frequency drift and more noise in oscillators, and lower sensitivity in sensors). The nonlinearities in piezoelectric LVRs will be discussed in the next section.

2.3 Nonlinearities in Piezoelectric LVRs

As discussed in the last section, nonlinearities greatly affect the performance of systems based on piezoelectric LVRs. In this section, the origins of nonlinearities will be first identified and examined. Techniques for reducing or harnessing nonlinearities will be introduced then.

2.3.1 Thermal Nonlinearity

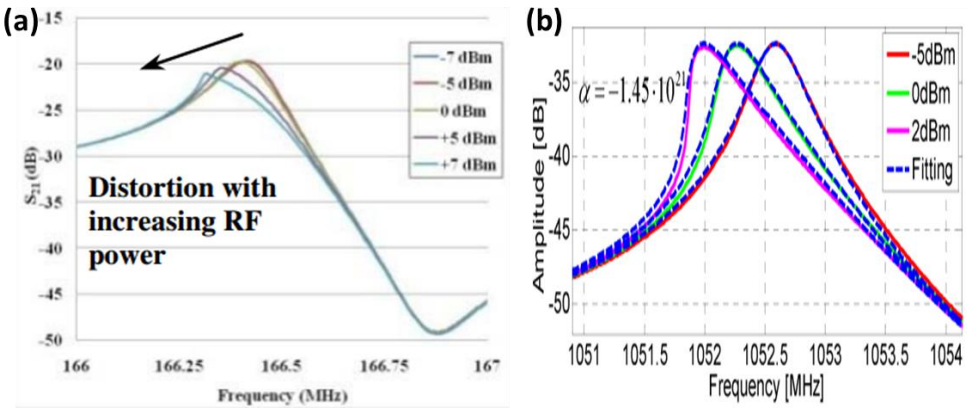

Figure 2.10 Thermal nonlinearity in piezoelectric LVRs. (a) GaN resonator [50]. (b) AlN resonator [60].

Thermal nonlinearity arises from the resonance drift caused by the joule heating and mechanical energy dissipation in the resonator. When thermal nonlinearity is dominant, typical admittance responses at different power levels are presented in Fig. 2.10 for GaN resonators [50] and AlN resonators [60]. Near the resonance, the admittance curve shifts to lower frequency due to the negative temperature coefficient of frequency (TCF) of the resonator [61]. Off the resonance, the thermal nonlinearity is not as obvious because the larger impedance leads to less energy dissipation and thus less temperature rise. It has been shown with a quantitative analysis based on Duffing equation approximation that thermal nonlinearity is the dominant nonlinearity in AlN LVRs [60]. However, the approach is only applicable to piezoelectric resonators with low k_t^2 at relatively low input power levels.

In this thesis, thermal nonlinearity will be proved as the main nonlinear effect in piezoelectric LVRs with quantitative discussions presented in Chapters 3 and 4.

2.3.2 Permittivity and Piezoelectric Nonlinearity

Although permittivity and piezoelectric nonlinearities have not been studied in piezoelectric LVRs, they have been investigated for AlN FBARs [62], [63]. They are represented as [62]:

$$D = \varepsilon^T E + dT + \varepsilon_2^T E^2 + d_2 T^2 + \varepsilon_3^T E^3 + d_3 T^3 \tag{2.11}$$

It is reported that these nonlinearities are no longer negligible when the E-field is larger than 15 V/μm in AlN FBARs [63]. Compared with FBARs, LVRs have much narrower thermal paths, so the thermal nonlinearity usually greatly distorts the frequency responses before permittivity and piezoelectric nonlinearities can be observed. Thus, these nonlinearities are not as critical as the thermal nonlinearity in LVRs.

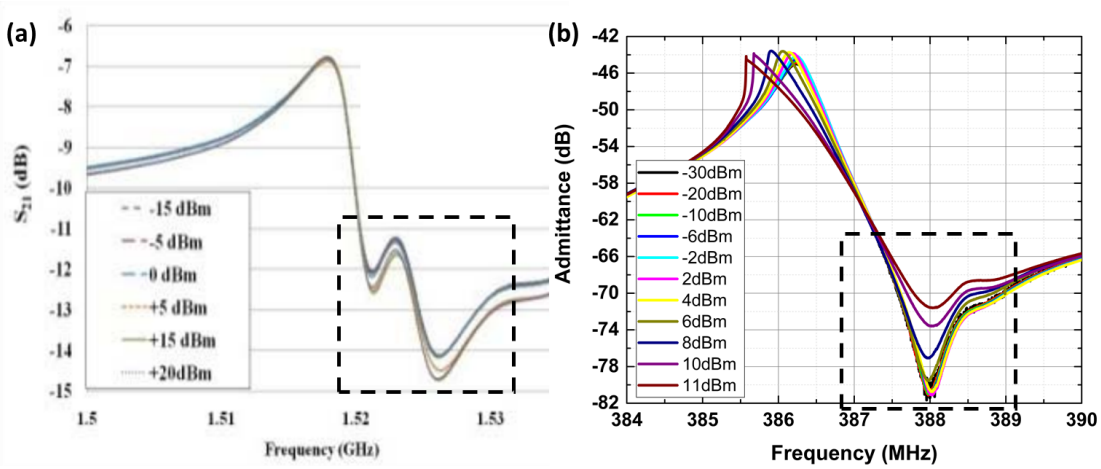

Figure 2.11 Nonlinearity near the anti-resonance caused by the substrate effect. (a) GaN resonator [50]. (b) AlN resonator.

2.3.3 Substrate Nonlinearity

Substrate nonlinear effect can also affect the performance of piezoelectric resonators. This is mainly caused by the doping in the substrate underneath the probing pads and piezoelectric thin film. At high power levels, the conductivity of the substrate becomes lower and thus another parasitic path is formed through the substrate, causing a higher admittance value near parallel resonance, as shown in Fig. 2.11. One method to reduce this substrate nonlinear effect is using substrates with higher resistivity.

2.3.4 Reducing and Harnessing Nonlinearities in Piezoelectric Resonators

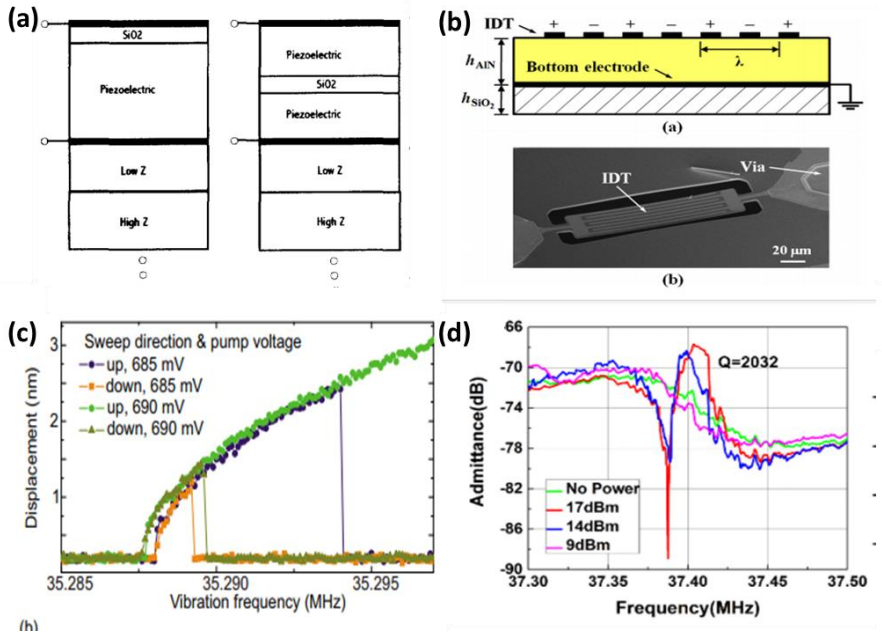

Figure 2.12 Piezoelectric resonator applications for reducing or harnessing nonlinearities. (a) Thermally compensated FBAR [64]. (b) Thermally compensated LVR [33]. (c) Resonant amplitude amplification due to nonlinear parametric amplification [65]. (d) *Q* enhancement leveraging parametric amplification [66].

Aside from studies aiming at identifying the origins of nonlinearities in LVRs, studies to reduce or to harness nonlinearities in piezoelectric LVRs have been reported. For applications susceptible to nonlinearities in LVRs (e.g. RF filtering front-ends), different techniques have been reported to reduce the dominant thermal nonlinearity [60]. SiO_2 thin film is used to compensate the negative TCF of AlN with its positive TCF both in FBARs [64] and LVRs [33]. Other approaches include modifying the geometry of the resonators to reduce heat accumulation in the resonant body [60].

Studies on harnessing nonlinearities in LVRs have just started to emerge. The nonlinearities in piezoelectric resonators, especially the parametric amplification phenomenon, can also be leveraged to achieve greater resonant amplitude [65], better *Q*, and lower phase noise [66]. Some of the reported applications are summarized in Fig. 2.12.

Chapter 3 Modeling of Thermal Nonlinearity and Intermodulation in Piezoelectric LVRs

In this chapter, a nonlinear MBVD model is shown first. Leveraging the nonlinear model and an iterative method, a numerical approach is presented to precisely model the thermal nonlinearities. Next, the intermodulation in resonators is introduced. Finally, based on the thermal nonlinearity model, an approach to accurately predict the intermodulation distortions in LVRs caused by thermal nonlinearity is presented.

3.1 Modeling of Thermal Nonlinearity in Piezoelectric LVRs

3.1.1 Nonlinear MBVD Model

As discussed in the last chapter, thermal nonlinearity originates from the resonance drift caused by the self-heating in the resonator. The resonance is approximated as [10]:

$$\omega_s = \frac{\pi}{W_e}\sqrt{\frac{E_{eq}}{\rho_{eq}}} \tag{3.1}$$

where ω_s is the resonance frequency, W_e is the width of pitch, E_{eq} and ρ_{eq} are the equivalent Young's modulus and density of the film stack forming the resonator respectively. When temperature rises, most materials (except a few materials like SiO_2 [64]) become softer, which is quantitatively described by negative temperature coefficient of elasticity (*TCE*) [33].

As a given power is applied to the resonator, the mechanical dissipation in the resonator manifests itself in heat, and introduces a temperature rise in the resonator body. Due to the negative *TCE* of piezoelectric material [61], the resonant frequency of LVRs exhibits a negative dependence on the temperature of the resonator, and can be formulated by [10]:

$$\omega_s(T) = \omega_{s0} \cdot (1 + TCF \cdot (T - T_0)) \tag{3.2}$$

where T and T_0 are the raised temperature and the room temperature, $\omega_s(T)$ and ω_{s0} are the shifted resonance and the resonance at room temperature respectively, and *TCF* is the resonator temperature coefficient of frequency. For AlN LVRs, the *TCF*s have been reported around -30

ppm/K [60]. For $LiNbO_3$ LVRs, the *TCF*s have been experimentally characterized, ranging from -85 ppm/K to -50 ppm/K for various orientations [45].

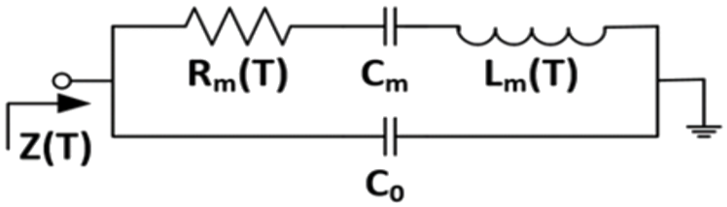

Figure 3.1 Nonlinear MBVD model for piezoelectric resonators.

Due to the resonance shifting, a nonlinear MBVD model, modified from the linear MBVD model, is introduced as shown in Fig. 3.1. Based on the linear MBVD model, which can accurately predict the resonator behavior in linear region, a nonlinear model is described as:

$$Z(T) = \frac{1}{j\omega C_0} // (R_m(T) + j\omega L_m(T) + \frac{1}{j\omega C_m}) \tag{3.3}$$

$$R_m(T) = \frac{\pi^2}{8} \cdot \frac{1}{\omega_s C_0} \cdot \frac{1}{k_t^2 Q} \tag{3.4}$$

$$L_m(T) = \frac{\pi^2}{8} \cdot \frac{1}{\omega_s^2 C_0} \cdot \frac{1}{k_t^2} \tag{3.5}$$

$$C_m = \frac{8}{\pi^2} \cdot C_0 k_t^2 \tag{3.6}$$

3.1.2 Modeling of Thermal Nonlinearity

The nonlinear MBVD model introduced in the last section depends on the temperature rise *T* in the resonator. To solve for the temperature rise, an investigation on the nonlinear process is first conducted. As depicted in Fig. 3.2, the thermally induced nonlinear process can be interpreted as the results of either a positive or a negative feedback for an excitation signal higher or lower than the resonant frequency. Figure 3.2 (a) - (c) show the positive feedback process when a high-power input RF signal is applied at a frequency lower than resonance. The heat generated causes a temperature rise and subsequently a resonance shift toward the lower frequency. It also leads to a larger admittance at the input frequency that in turn enables higher power absorption into the resonator body and produces further resonance downward shift. This nonlinear process eventually converges as the temperature (*T*) saturates and reaches equilibrium. A negative feedback process

is presented in Fig. 3.2. (d) - (f) when a high-power input RF signal is exerted at a frequency higher than resonance. The temperature rise induced by accumulated heat shifts the resonance toward the lower frequency, which causes a smaller admittance and less dissipated heat. The negative feedback will also reach to equilibrium. The convergence of the temperature is dictated by thermal dynamics of the resonator structure and described by the following equation:

$$\left|\frac{V_r}{Z}\right|^2 \cdot Re[Z(T)] - n \cdot \frac{T-T_0}{R_{th}} = C_{th} \cdot \frac{dT}{dt} \tag{3.7}$$

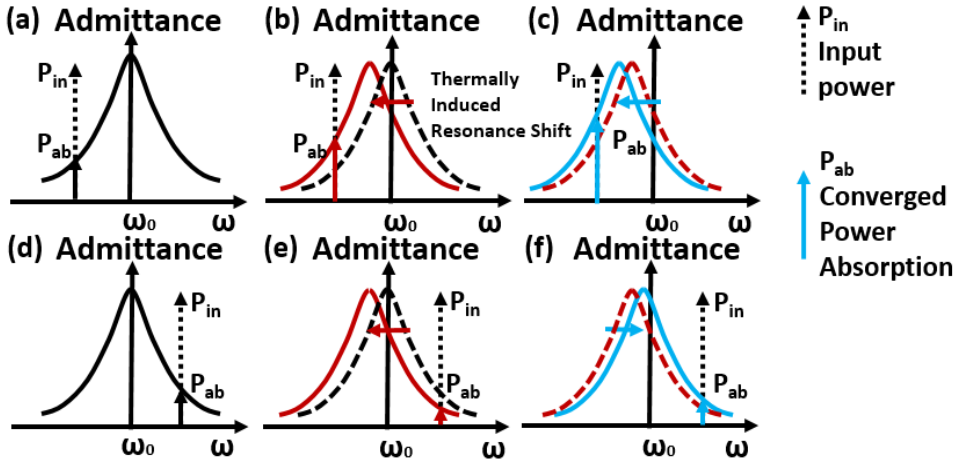

Figure 3.2 Conceptual explanation of the nonlinear distortion in resonator admittance response. (a) - (c) Positive feedback. (d) - (f) Negative feedback.

The first term in Eq. 3.7 is the joule heating generated in the resonator assuming all dissipated energy is converted to heat. V_r is the voltage applied across the resonator, and $Z(T)$ is resonator's input impedance as a function of resonator temperature described by the nonlinear MBVD model (Eq. 3.3 – 3.6).

The second term in Eq. 3.7, in which n is the number of anchors, and T-T_0 is the difference between the raised temperature and the room temperature, embodies the heat escaping the resonator via the anchors. R_{th} is the thermal resistance of individual anchors, related with the physical dimensions and material properties as [60]:

$$R_{th} = \frac{L_{metal}}{\kappa_{metal} \cdot W_{metal} \cdot D_{metal}} \;//\; \frac{L_{piezo}}{\kappa_{piezo} \cdot W_{piezo} \cdot D_{piezo}} \tag{3.8}$$

where L, W, and D are dimensions of each material layer in the anchor. κ is the material thermal conductivity. The thermal resistance of the anchors can be considered as two thermal resistances

connected in parallel.

The third term is the transient stored heat, and C_{th} is the thermal capacitance of the resonator, defined as [60]:

$$C_{th} = \rho_{metal} \cdot V_{metal} \cdot C_{metal} + \rho_{piezo} \cdot V_{piezo} \cdot C_{piezo} \tag{3.9}$$

where ρ, V and C_p are the density, volume and specific heat of each layer. The total thermal capacitance of the device structure is the sum of the thermal capacitances stemming from the metal electrodes and the piezoelectric material.

Based on the aforementioned nonlinear model, Eq. 3.7 is enough for solving the thermal nonlinearity in piezoelectric LVRs. However, directly solving the equation leads to an expression which can be approximated by the Duffing equation [29] when temperature variation is small. To get an accurate prediction of the thermal nonlinearity, a numerical method is adopted, which will be discussed in the next section.

3.1.3 Numerical Method for Thermal Nonlinearity

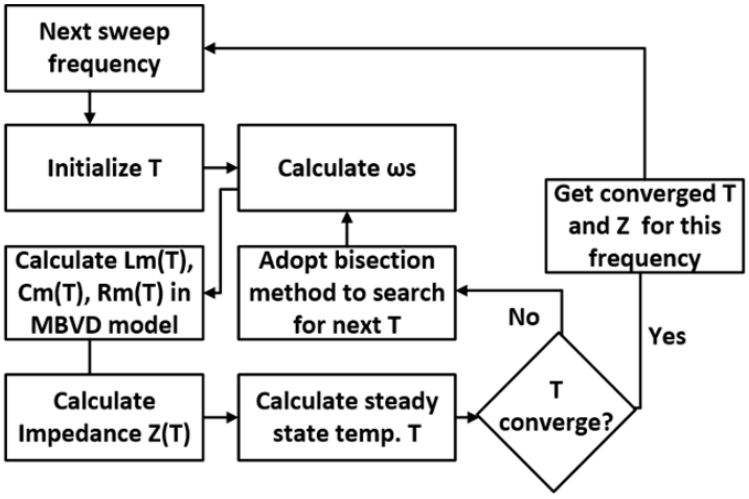

Figure 3.3 The iterative procedure for numerically simulating the thermal nonlinearity in piezoelectric LVRs.

Utilizing the parameters in a MBVD model that accurately describes resonance response in the linear region, we can prepare the beginning of an iterative procedure shown in Fig. 3.3. In the first iteration for each excitation frequency, the temperature rise is set to either 0 or the converged T value derived from iterations for the prior frequency. The method then starts with calculating the

resonant frequency for this initialized temperature. Subsequently, the resonator impedance at the excitation frequency is calculated with the MBVD model that is dependent on the resonance. The real part of the impedance introduces joule heating and represents mechanical power dissipation, and leads to a temperature increase that can be solved with a thermodynamic equation for the resonator. This procedure is iterated until the temperature variation in the resonator converges. The converged temperature is then used in the MBVD model to compute the admittance at the given frequency. To attain the nonlinear admittance response over a wide frequency range, this algorithm is repeated for each excitation frequency.

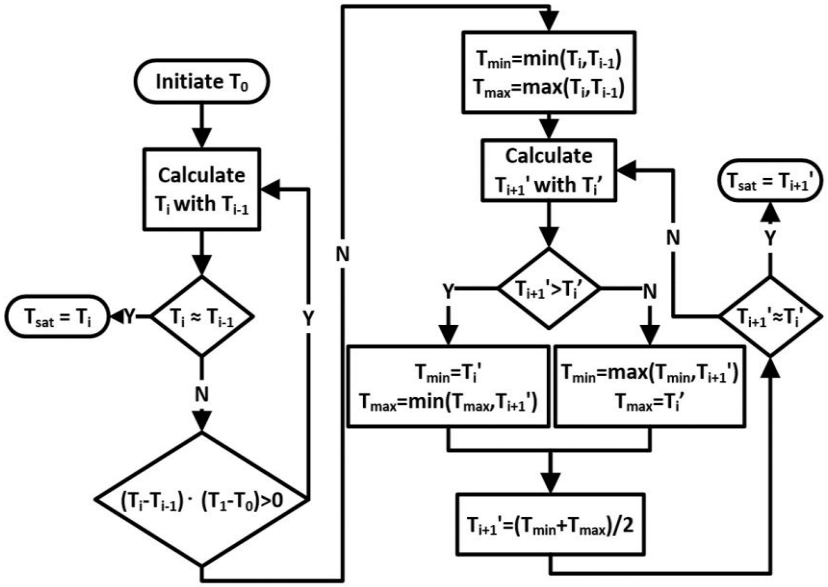

Figure 3.4 Bisection method for seeking convergence.

For excitation frequencies close to the resonance, the thermally induced admittance variation will be much more radical due to the high *Q* of the resonator. A merely recursive method cannot guarantee convergence in iterations. Results of iterations can be driven into an oscillation between two temperatures, neither of which is the converged value. In this case, the bisection method [67] is adopted to ensure that iterations progress toward the convergence, as seen in Fig. 3.4. The calculation is finished by a Mathematica code. More details are included in Appendix A.1.

3.2 Modeling of Intermodulation in Piezoelectric LVRs

Thermal nonlinear, modeled in the last section, is not the only concern when designing an RF system. Moreover, intermodulation distortion (IMD) is another important characteristics for

describing linearity for a wide range of microwave and RF components [68]. This section emphasizes on examining the origin of IMD and accurately modeling IMD in piezoelectric LVRs.

3.2.1 Intermodulation Distortion

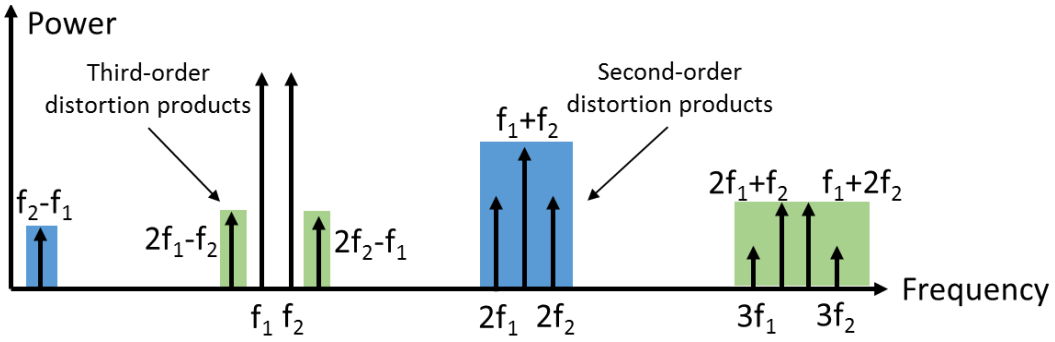

Figure 3.5 Typical intermodulation distortions.

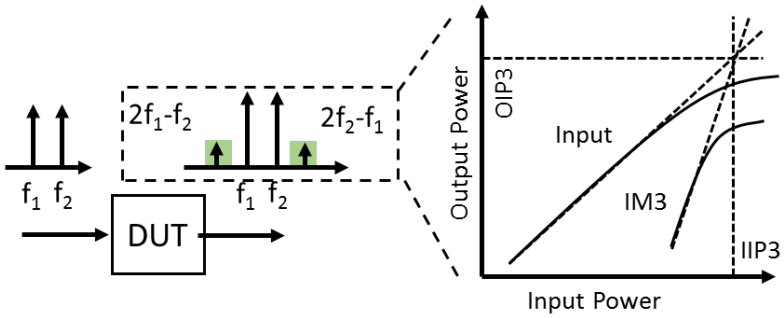

Figure 3.6 Definition of IMD3.

The IMD originates from the injection of a two-tone signal (f_1 and f_2) into the device under test (DUT). For an ideal linear device, the output signal only contains f_1 and f_2. However, a realistic component with certain level of nonlinearity will produce signals at other frequencies. These signals include the harmonics of the original (named as n^{th} order harmonics at n-time frequencies of the fundamental tones) and the intermodulation between the two-tones. The intermodulation signals are sorted into different orders as seen in Fig. 3.5.

Two of the most challenging distortion products for RF applications are the third-order distortion (IMD3) products near the original two-tone signals ($2f_1$-f_2 and $2f_2$-f_1). It is because third-order distortion products create additional frequency content near the modulated signal (called spectral regrowth [68]). The spectral regrowth caused by poor linearity interferes other wireless channels.

Besides, for two-tone signals with small frequency spacing, IMD3 are difficult to remove with filters.

To quantitatively describe IMD3, third order intercept points (TOIs) are defined for both third-order input intercept point (IIP3) and third order output intercept point (OIP3) as shown in Fig. 3.6.

For piezoelectric MEMS resonators, the IMD3 has been experimentally tested on FBARs [69] and LVRs [60], [70] (Fig. 3.7). It is reported that severe IMD3 is one of the biggest hurdles for commercially adopting LVRs as RF front-ends [60]. However, this issue has never been quantitatively studied. An accurate model is needed for optimizing the performances of LVRs.

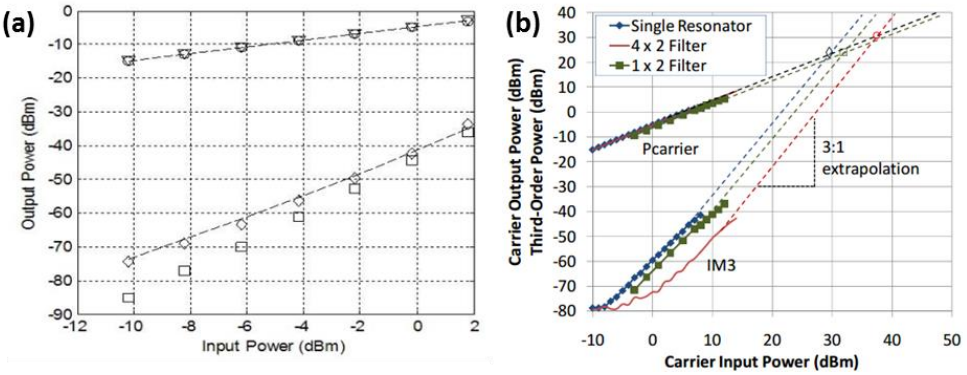

Figure 3.7 Reported IMD3 in piezoelectric (a) FBARs [69] and (b) LVRs [70].

3.2.2 Modeling of Thermally Induced Intermodulation in LVRs

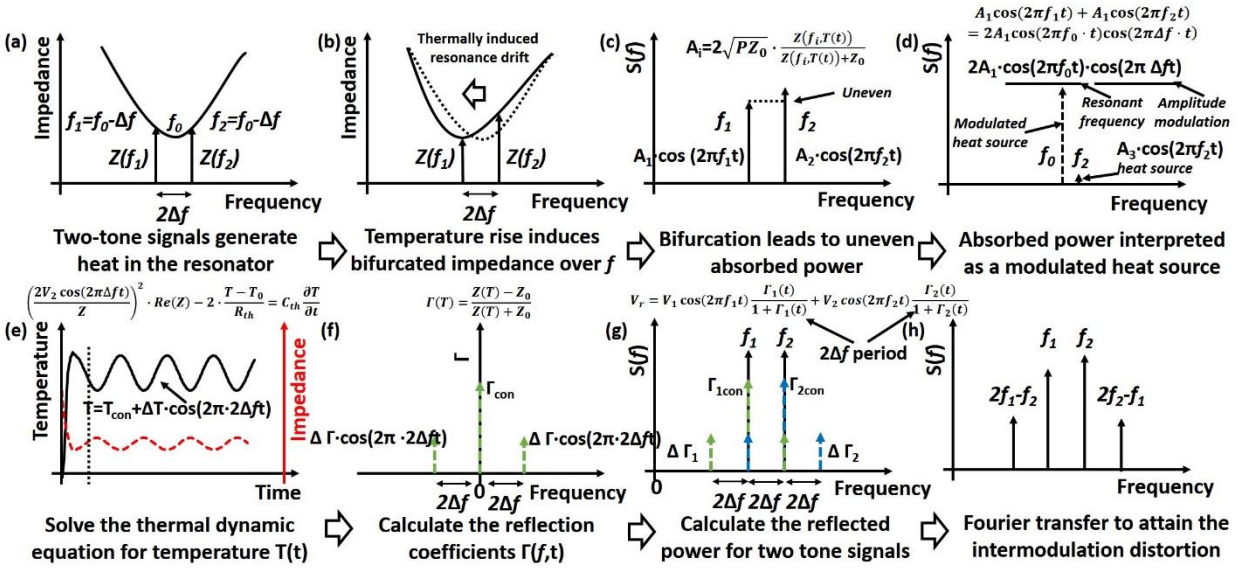

Figure 3.8 Method for quantitatively characterizing the IMD3 in AlN LVRs. (a) Two tones with equal spectral spacing to the resonance are used in IMD3 measurement. (b) Resonance bifurcation caused by the absorbed power and subsequently produced heat. (c) Bifurcation-induced unequal impedances, reflection coefficients, and absorbed power. (d) Combined absorbed power interpreted as an AM signal source and a constant signal source. (e) Temperature variation and impedance fluctuation at a given frequency solved using thermal dynamics of the resonator. (f) Calculated reflection coefficients in both the time and frequency domains. (g) Spectral analysis of the reflected signals and the contributing terms of IMD3. (h) Fourier transform results of reflected signals.

Based on the thermal nonlinearity model described in section 3.1, a model for thermally induced intermodulation in LVRs is achieved. It is worth noting that Eq. 3.3 is modified for excitations at different frequencies:

$$Z(f,T)=\frac{1}{j2\pi f C_0}//(R_m(T)+j2\pi f L_m(T)+\frac{1}{j2\pi f C_m}) \tag{3.10}$$

As depicted in Fig. 3.8(a-b), upon the excitation from two tones at f_1 and f_2, the mechanical energy dissipation in the resonator produces joule heating and causes the resonance to bifurcate. The bifurcation [Fig. 3.8(c)] leads to unequal impedances presented to the two tones and induces uneven power absorption. The even parts of the two tones can be combined and interpreted as an amplitude modulated (AM) heat source while the uneven portion is considered as a constant heat source [Fig. 3.8(d)]:

$$\begin{aligned} V_{inc} &= A_1\cos(2\pi f_1 t)+A_2\cos(2\pi f_2 t) \\ &= 2A_1\cos(2\pi f_0\cdot t)\cos(2\pi\Delta f\cdot t)+(A_2-A_1)\cos(2\pi f_2 t) \end{aligned} \tag{3.11}$$

where V_{inc} is the total incident signal of the resonator. A_i is the amplitude of the incident signal of each source and can be formulated by:

$$A_i = 2\sqrt{PZ_0} \cdot \frac{Z(f_i, T(t))}{Z(f_i, T(t)) + Z_0} \tag{3.12}$$

where P is the RF power provided by the sources and Z_0 is the characteristic impedance of the system. The modulation frequency (f_1 - f_2) of the heat equates the spectral difference between the two tones.

The resonator temperature, varying in time, can be solved with the thermal dynamic equation:

$$\left|\frac{V_{inc}}{Z}\right|^2 \cdot Re[Z(f,T)] - n \cdot \frac{T-T_0}{R_{th}} = C_{th} \cdot \frac{dT}{dt} \tag{3.13}$$

which is similar to Eq. 3.7. The first term in Eq. 8 is the joule heating assuming all dissipated energy in the resonator is converted to heat. $Z(f,T)$ is the impedance corresponding to the signal frequency at certain temperature T defined by Eq. 3.10. The second term embodies the heat escaping the resonator via the anchors. R_{th} is the thermal resistance of an individual anchor defined by Eq. 3.8 with the physical dimensions and material properties. The third term is the transiently stored heat that can determined by the thermal capacitance (C_{th}), defined in Eq. 3.9, and temperature variation rate of the resonator.

Naturally, the temperature variation would follow an amplitude modulation ($2\Delta f$ in Eq. 3.11) that is lower than or comparable to the resonator thermal frequency ($1/\tau_{thermal}$). Due to the dependence of resonance on temperature, the second order effect of the temperature variation would manifest as impedance fluctuations near the resonance, introducing time-varying reflection coefficients (modulated at f_1 - f_2) at the input of the resonator [Fig. 3.8(e)]. Consequently, the reflected waves [Fig. 3.8(f-g)], a mixing product of the reflection coefficients (f_1 - f_2) and input tones (f_1 and f_2), feature IMD3 at $2f_1$-f_2 and $2f_2$-f_1:

$$V_{refl} = A_1 \cos(2\pi f_1 t) \frac{\Gamma_1(t)}{1+\Gamma_1(t)} + A_2 \cos(2\pi f_2 t) \frac{\Gamma_2(t)}{1+\Gamma_2(t)} \tag{3.14}$$

$$\Gamma(T) = \frac{Z(f,T) - Z_0}{Z(f,T) + Z_0} \tag{3.15}$$

where V_{refl} is the reflected power, and Γ is the reflection coefficient.

To predict the IMD3 quantitatively, the thermally influenced parameters, including resonance, impedance, temperatures, and reflection coefficients, are holistically solved in the time domain, before fast Fourier transform is performed to extract the spectral density of the reflected signals [Fig. 3.8(h)]. The analysis of the intermodulation term is achieved by a Matlab code, as shown in Appendix B.

Chapter 4 Experimental Validation

In this chapter, experimental validation of the theoretical analysis is presented. The experimental validation is conducted on both AlN and $LiNbO_3$ devices. The linear responses of DUTs are first measured. The thermal nonlinearity model is then verified with measurement. Next, IMD3 are measured and compared with the model provided in Chapter 3. Finally, discussions of thermal nonlinearities and IMD3 are presented.

4.1 Devices under Test and Measurement Setup

4.1.1 Linear Response of DUT

Both AlN and $LiNbO_3$ LVRs were fabricated in the cleanroom. The fabrication process for AlN resonator is described in [71] while that for $LiNbO_3$ resonators is discussed in [61]. The SEM images of the fabricated devices are shown in Fig. 4.1.

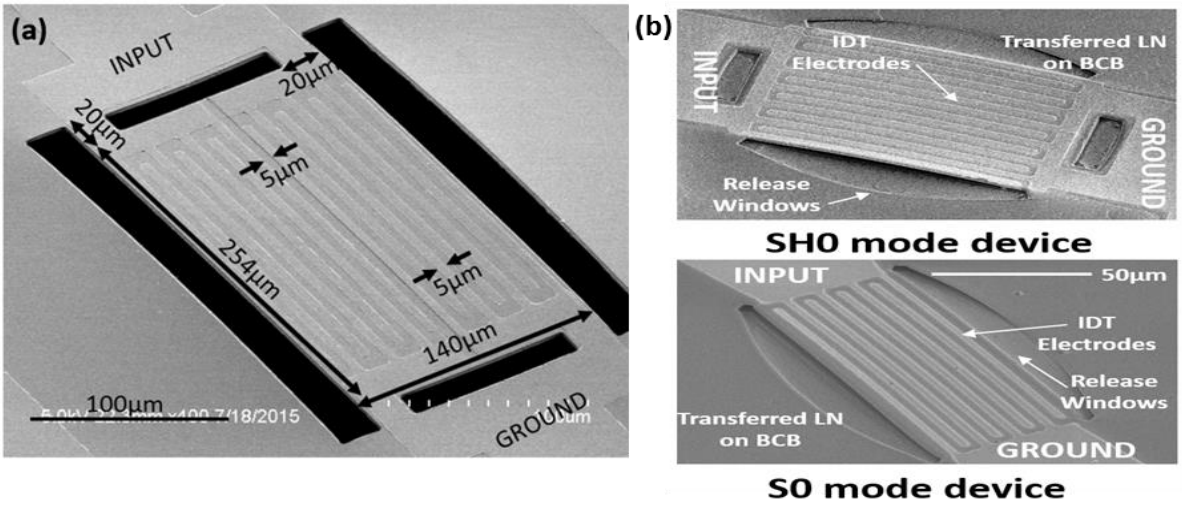

Figure 4.1 Fabricated AlN resonators [71] and $LiNbO_3$ resonators [61].

The linear responses of DUTs were measured with an Agilent 5230A PNA-L Network Analyzer and a probe station. First, a 456 MHz and a 566 MHz device are measured in vaccum and fitted with MBVD model described in section 2.1. The measurement was carried out at -10 dBm power level which is in the linear regime of the resonator. The responses are presented in Fig. 4.2 and Table 4.1.

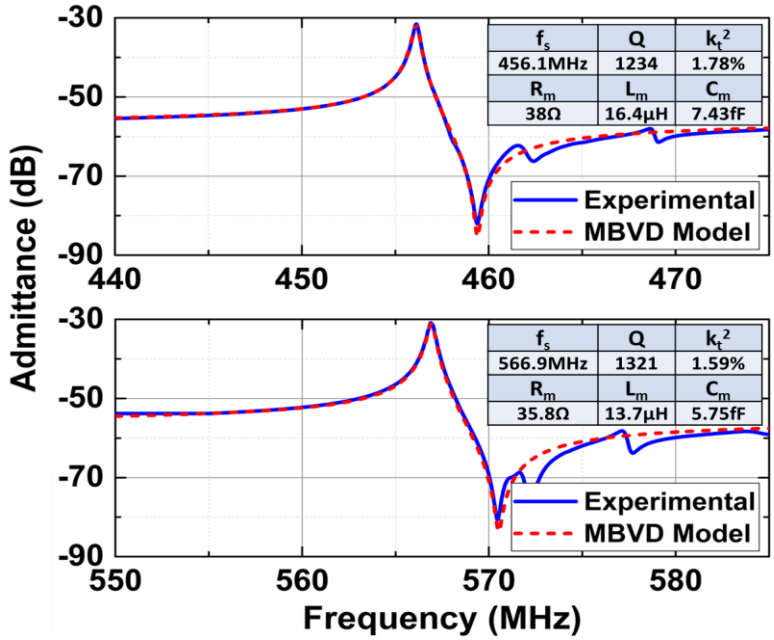

Figure 4.2 Measured spurious mode-free AlN resonators in vacuum. (a) 456 MHz resonator. (b) 566 MHz resonator.

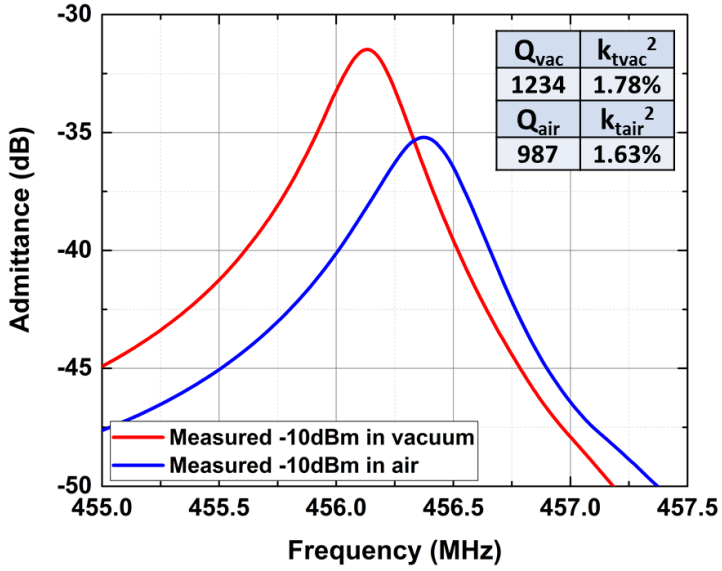

Figure 4.3 Measured 456 MHz spurious mode-free AlN resonator (a) in vacuum and (b) in air.

Next, the frequency response of the resonator was also measured in air and compared with the performance in vacuum in Fig. 4.3 and Table 4.1. The results show a significant decrease in *Q*, which is caused by more damping in air, described by [72]:

$$\frac{1}{Q_{air}} = \frac{1}{Q_{air\_damping}} + \frac{1}{Q_{vac}} \tag{4.1}$$

where Q_{air} is the quality factor in air, $1/Q_{air\_damping}$ represents the energy loss due to air damping, Q_{vac} is the quality factor in vacuum considering anchor losses, electrical loadings, etc.

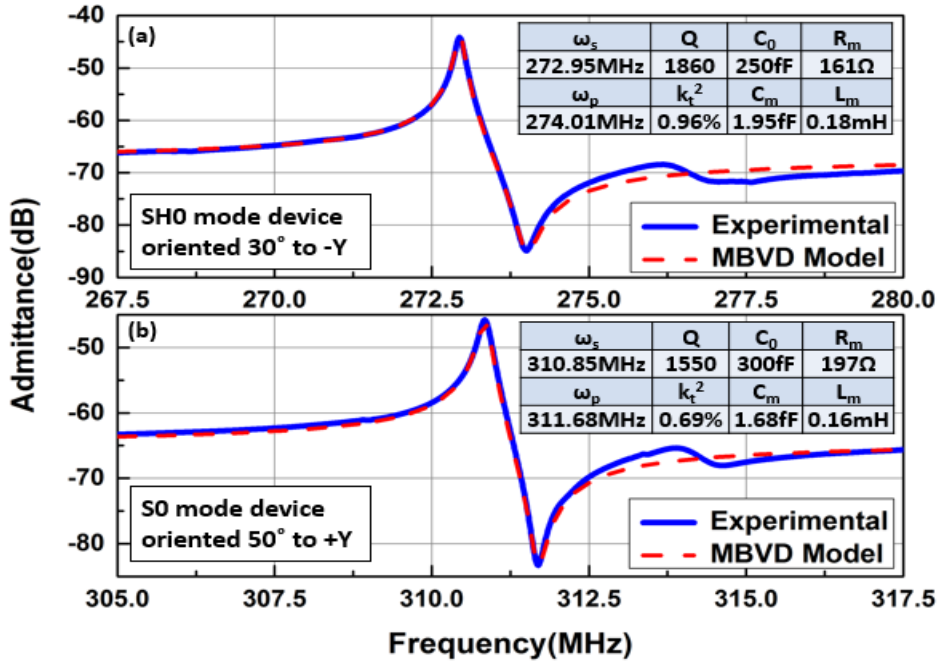

Figure 4.4 Measured $LiNbO_3$ resonators. (a) SH0 mode device oriented 30° to –Y axis. (b) S0 mode device oriented 50° to +Y axis.

Table 4.1 Extracted linear performance from measured piezoelectric LVRs.

No.	Material	Condition	k_t^2	Q	f_s
1	AlN	Vacuum	1.78%	1234	456.1MHz
2	AlN	Vacuum	1.59%	1321	566.9MHz
1 (air)	AlN	Air	1.63%	987	456.4MHz
3	$LiNbO_3$	Air	0.96%	1860	272.9MHz
4	$LiNbO_3$	Air	0.69%	1550	310.9MHz

Third, $LiNbO_3$ resonators, both S0 and SH0 devices were tested in air, as shown in Fig. 4.4. The extracted MBVD key parameters of the tested devices are presented in Table 4.1.

4.1.2 Thermal Nonlinearity and IMD3 Measurement Setup

The thermal nonlinearity was measured with an Agilent 5230A PNA-L Network Analyzer at different input power levels. The power level is controlled by the power source in the VNA.

Forward frequency sweep and backward frequency sweep were set by choosing the sweeping either from low to high frequency or high to low frequency respectively. The sweeping time was controlled to be long enough for the system to reach equilibrium.

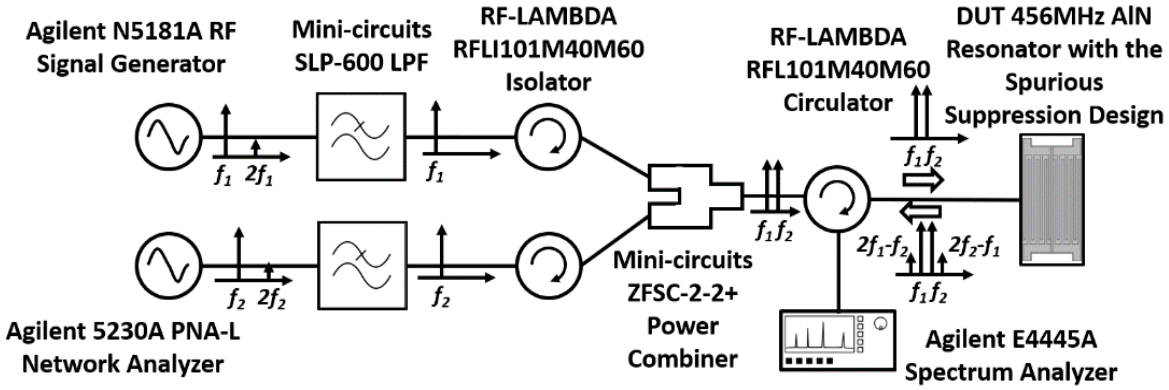

Figure 4.5 IMD3 measurement setup.

The IMD3 measurement setup is shown in Fig. 4.5. The low-pass filters and isolators were used to attenuate higher order harmonics of the sources and suppress the IMD3 caused by measurement setup other than the DUT.

4.2 Comparison of Measurement and Theory

4.2.1 Comparison of Thermal Nonlinearity Results

Based on the linear responses reported in the last section and the model in Chapter 3, thermal nonlinearities were calculated and compared with measurement. The thermal resistances of different resonators were first calculated with Eq. 3.8. The physical dimensions were set by the design [71], [73]. The thermal conductivities of metal layers (Al and Au layer) were obtained from [74]. The thermal conductivity of AlN was obtained from [75]. For piezoelectric $LiNbO_3$ thin film, the thermal conductivity was reported in [76]. Detailed values used in the calculation are presented in Table 4.2.

Using the thermal nonlinearity model described in Chapter 3, the thermal nonlinear behaviors were modeled and compared with the measurements. First, AlN resonators at 456 MHz and 566 MHz were measured in vacuum condition. The results are presented in Fig. 4.6. The calculated and measured R_{th} are also presented.

Table 4.2 Key parameters for calculating thermal resistance R_{th}.

No.	Unit	1	*2*	3	4
L_{metal}	μm	18	16	20	60
κ_{metal}	W/(m·K)	205	205	205	205
W_{metal}	μm	17.5	14	5	25
D_{metal}	μm	0.15	0.15	0.15	0.15
L_{metal}	μm	18	16	40	60
κ_{piezo}	W/(m·K)	48.1	48.1	4.18	4.18
W_{piezo}	μm	21.5	18	5	25
D_{piezo}	μm	1	1	1	1
n	1	4	4	4	2
R_{th}	K/W	2862K/W	3086K/W	27510K/W	33000K/W

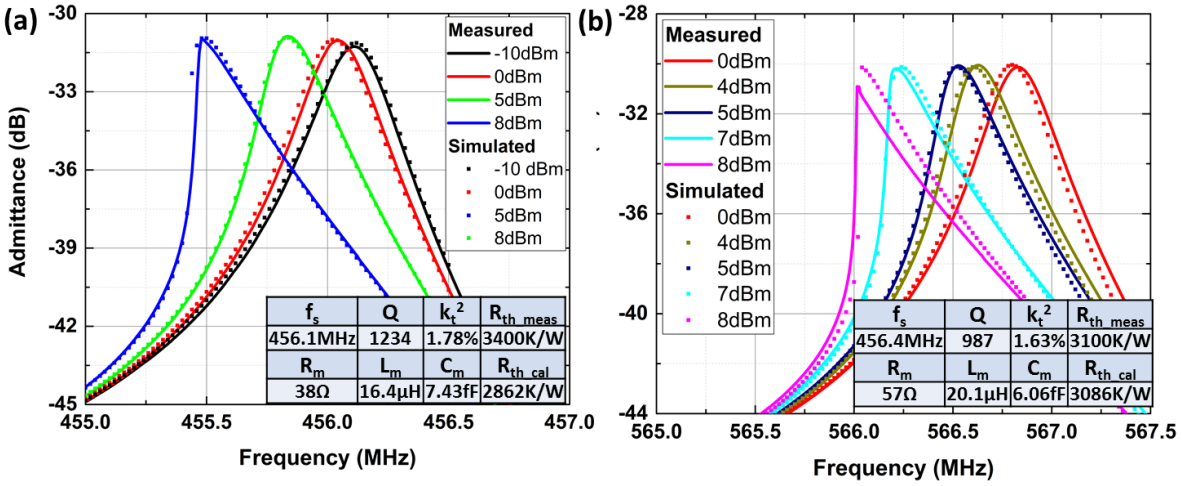

Figure 4.6 Measured and simulated nonlinearity of a (a) 456 MHz AlN resonator and (b) 566 MHz AlN resonator.

Second, the influence of air ambience to the thermal conductivity was investigated (Fig. 4.7). The thermal convection process conducts a portion of the accumulated heat and thus generates a smaller equivalent thermal resistance. Measured thermal resistance in air is around half of that measured in vacuum for the 456 MHz AlN design (1750 K/W in air compared with 3400 K/W in vacuum).

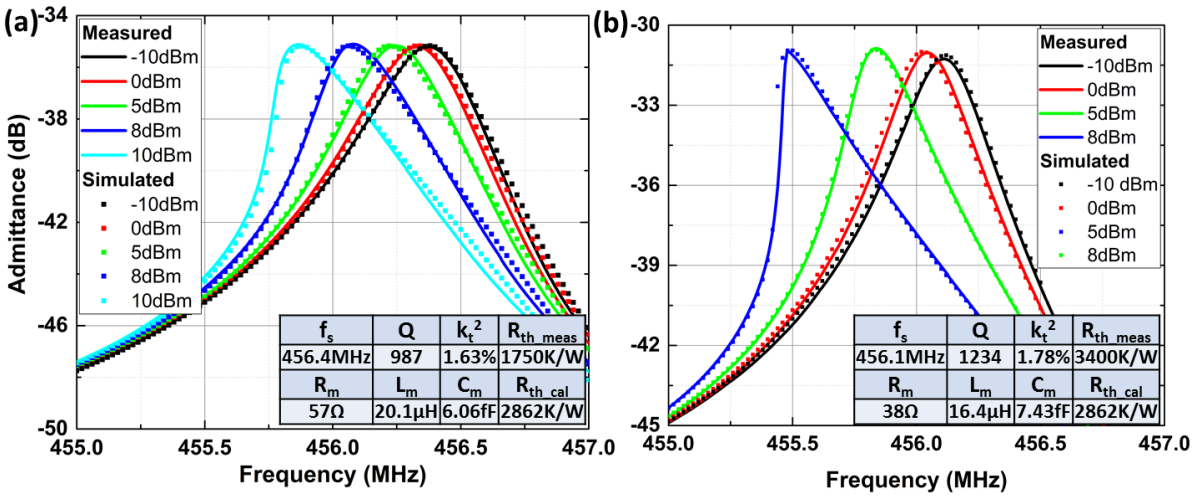

Figure 4.7 Measured and simulated nonlinearity of a 456 MHz AlN resonator (a) in air and (b) in vacuum.

Third, forward and backward sweep were conducted on $LiNbO_3$ resonators. The bifurcation response shown in Fig. 4.8 is commonly observed for resonant systems bearing nonlinearity, and its origin can be mathematically explained. Bifurcation occurs when the input signal of sufficiently high power gives rise to two viable solutions for the equilibrium resonator temperature near resonance. Further increase in the power can result in three solutions for the equilibrium resonator temperature. The resonator temperature can only stabilize to one of the solutions, and the process is determined by the prior condition of the resonator. Forward and backward frequency sweeps impose different prior conditions for capturing bifurcation phenomena, and therefore lead to different stabilized temperatures and response near the bifurcated resonance. For example, a backward sweep approaching bifurcation point would have a higher prior temperature than that for a forward sweep approach bifurcation from the opposite direction. The resonator temperature converges to the solution closer to its prior condition in bifurcation frequency range during forward and backward frequency sweeps. Away from the frequency range over which the admittance response bifurcates, there will be only one equilibrium solution. Thus, the response is identical for two sweep types.

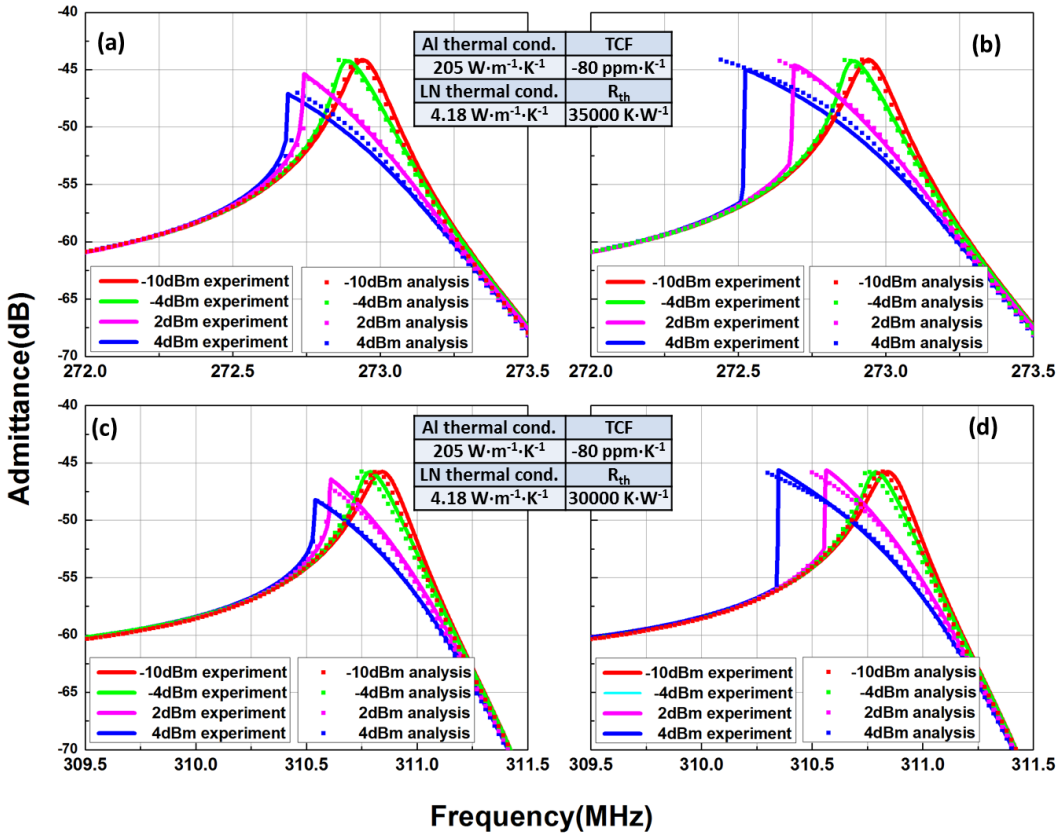

Figure 4.8 Comparison between the simulated nonlinearity response and measured results at different power levels. (a), (b) Forward and backward frequency sweep for the SH0 mode device. (c), (d) Forward and backward frequency sweeps for the S0 mode device.

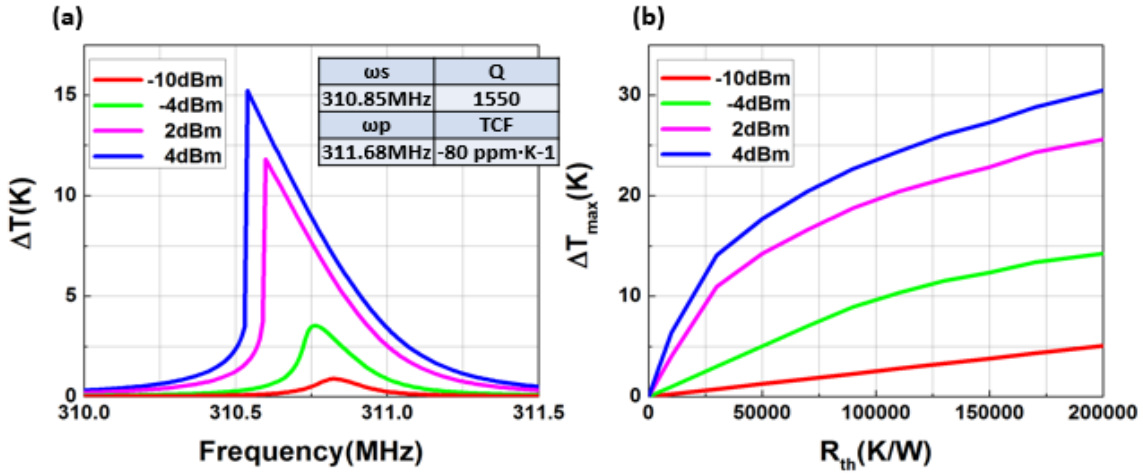

Figure 4.9 (a) Simulated temperature response at different power levels for the S0 mode device at forward sweep. (b) Maximum temperature increase vs. thermal resistance at different power levels for the S0 mode device.

The method described herein is also extended in Fig. 4.9 (a) to show the temperature rise (ΔT) in the S0 mode resonator at various excitation frequencies around the resonance. It is expected that

higher excitation power gives rise to a larger temperature variation and consequently more severely distorted admittance response from the linear regime. For the S0 mode device under forward sweep test of 10 dBm power, the resonator temperature rises by 15 K. The temperature rises with respect to input power. For 20 dBm back-sweep signal, the maximum temperature rise can reach 91 K. The interdigitated electrodes made of Al would degrade due to the accelerated oxidation of Al in high temperature and dry air ambience.

As shown in Fig. 4.9 (b), the maximum ΔT for the S0 mode resonator, defined as the peak equilibrium temperature in Fig. 4.9 (a), is also theoretically investigated for its dependence on the thermal resistance associated with the anchors. It is important to note that thermal nonlinearity can be suppressed by reducing the thermal resistance associated with anchors and hastening the heat conduction out of the resonator.

4.2.2 Comparison of IMD3 Results

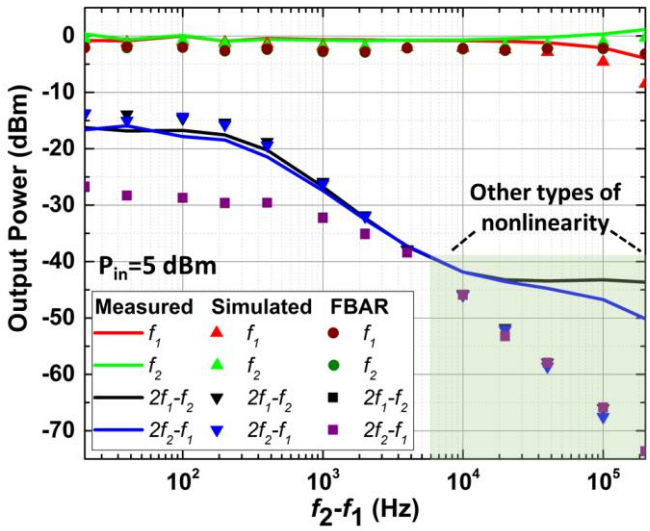

Figure 4.10 Measured and simulated IMD3 at various frequency differences and input power of 5 dBm.

First, a 456 MHz AlN resonator was measured in air condition with two tones at various frequency differences and a fixed input power of 5 dBm. Using the described quantitative method, the measured and calculated IMD3 at various frequency differences are presented in Fig. 4.10. An excellent agreement is obtained between the measurements and simulations. The simulation was done with R_{th}=1750 K/W, C_{th}=30·10^{-8} J/K, k_t^2=1.63%, and Q=987. Because the measurement was done in room temperature and dry air ambiance, the calculation of C_{th} includes contribution from

the air surrounding the resonator.

The high IMD3 products for Δf smaller than the thermal frequency can be attributed to the larger temperature variation (Fig. 4.11). As seen in Fig. 4.11, the frequency of envelope modulation, $2\Delta f$, introduces much larger time-varying temperature fluctuation in the resonator when it is much smaller than the thermal frequency. The increase in Δf would cause a decrease in the amplitude of temperature variation as the thermal response struggles to follow the electrical excitation. The phenomenon leads to the diminishing of IMD3 at larger Δf. A sufficiently large Δf would eventually result in IMD3 in the resonator predominantly produced by other types of nonlinearity.

The simulated response of a typical fully anchored FBAR with similar characteristics is also included for comparison with AlN LVRs (R_{th}=350 K/W, C_{th}=30·10^{-8} J/K, k_t^2=5%, Q=987). It is clear that FBARs outperform LVRs in linearity at low Δf due to their lower thermal resistance and subsequently higher thermal time constant.

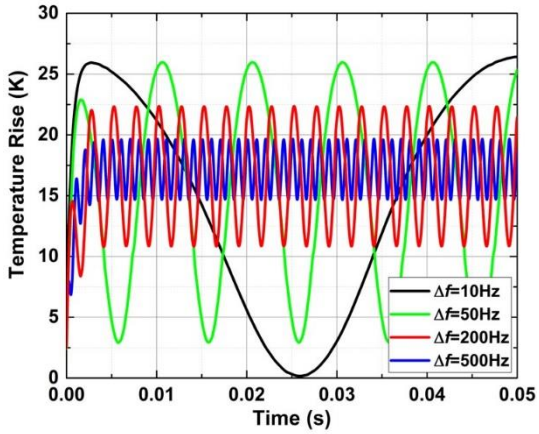

Figure 4.11 Simulated resonator temperature variations in time domain for different values of Δf.

Second, the IMD3 at different input power levels with the same Δf was measured. The measurements are compared with simulations in Fig. 4.12. The discrepancy between simulations and measurements stems (shown in the highlighted region) from the fabricated device having lower Q at low power levels. This phenomenon, in which Q decreases at low power level, was observed in multiple fabricated AlN devices, and its origin is still under investigation.

It is noteworthy that the measured curves are different from typical IMD3 curves measured in filters. As the input power increases, the slope of IMD3 terms is not 3 times of the slope of the input two-tone signal. The reason is that the reflection power instead of the transmitted power is

measured since the resonator is a one-port device. An extended simulation is shown in Fig. 4.13. At low power level, larger input power generates greater temperature variation and thus leads to a rise in the IM3 of the reflected signal. However, at high input power level, the increase in IM3 products gradually saturates, because at high input power level, although the temperature variation is still large, the highly bifurcated impedance curve fails to provide enough difference in the reflection coefficient caused by the temperature fluctuation. Thus, the IM3 products in the reflected power gradually saturate.

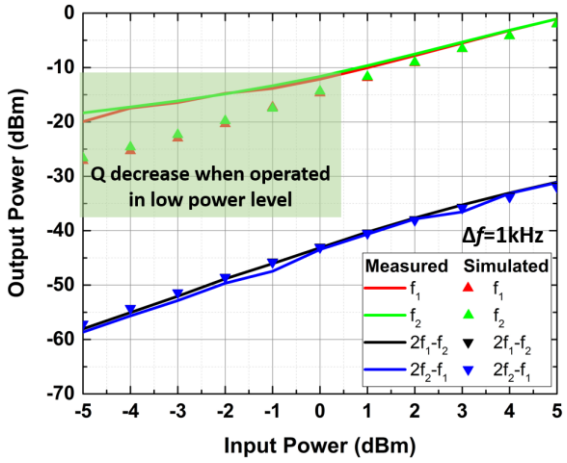

Figure 4.12 Measured and simulated IMD3 at different input power levels and a frequency difference of 2 kHz.

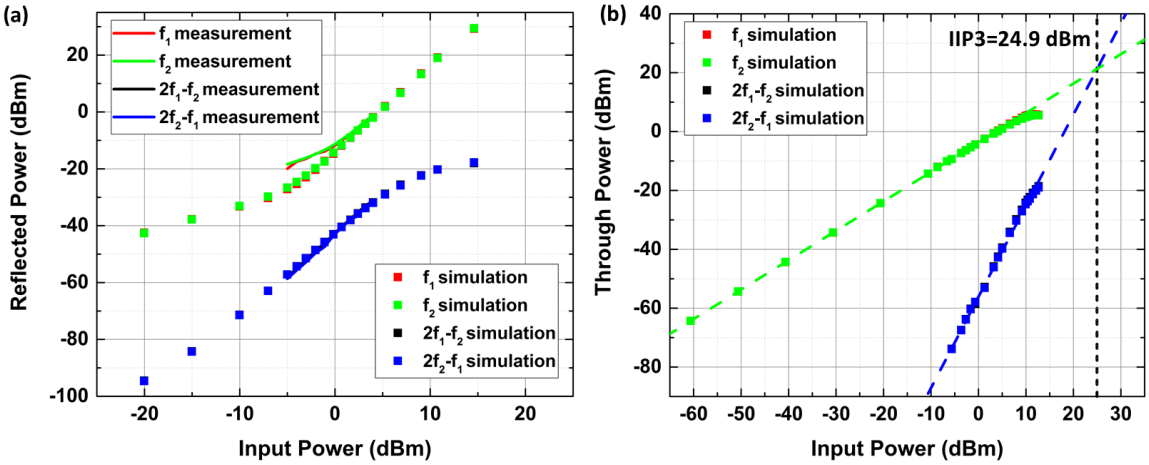

Figure 4.13 (a) Measured and simulated reflected power (including two-tone signals and IMD3 products) for the AlN LVR with different input power. (b) Simulated transmitted power of the AlN LVR with different input power when the ground is terminated with a receiving port.

For a better comprehension of the IMD3, a simulation for the transmitted power is shown in Fig.

4.13 (b). The simulation assumes the same DUT but terminates the ground of the resonators with another 50Ω termination, thus it becomes a virtual two-port device. We can clearly observe that the three times relation in the slopes of the first order term and IMD3 products. The IIP3 is calculated to be 24.9 dBm implying the limited power handling ability of the current LVR designs.

Third, the impact of surrounding air on the thermal resistance and thermal capacitance was also investigated. The same device was measured in vacuum for comparison. The results indicate that surrounding air creates a thermal pass (smaller R_{th}) and absorbs certain amount of heat (larger C_{th}). A quantitative study is presented in Fig. 4.14. The air ambiance causes a smaller intermodulation in general.

In conclusion, it can also be observed that thermal nonlinearity is dominant for intermodulation within 10 kHz. Other nonlinearities (likely mechanical nonlinearity) cannot be ignored for large intermodulation spacing or small input power (although usually insignificant). The study of other nonlinearities and their impact on IMD3 in LVRs is still inconclusive.

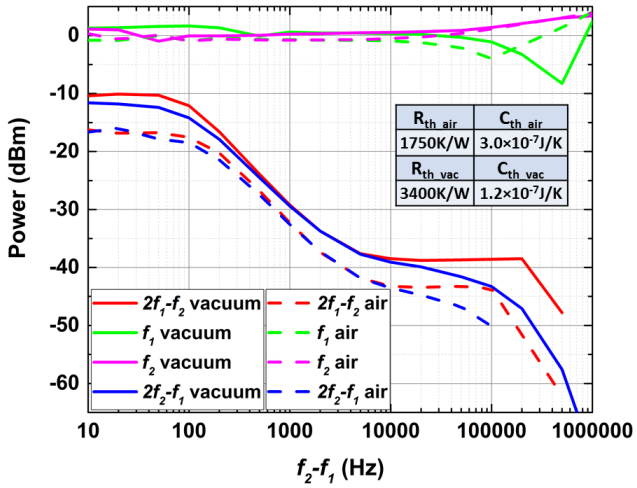

Figure 4.14 Measured and simulated higher-order intermodulation products of the AlN LVR.

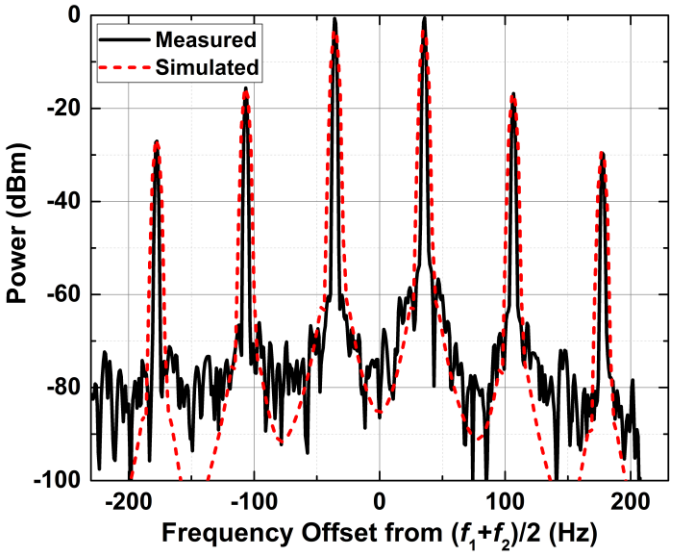

Figure 4.15 Measured and simulated higher-order intermodulation products of the AlN LVR.

Furthermore, the intermodulation model is generalized for higher-order harmonics. Higher-order harmonics cannot be ignored when the frequency spacing between two tones is close or the two-tones are at high power level. As seen in Fig. 4.15, the measured spectral density of the reflected signals is also precisely predicted by our quantitative method up to the 5th order. The simulation was done using Fourier transform with the Blackman window function to reduce the influence of the spectrum leakage (side lobes in the spectrum).

Chapter 5 Conclusion and Future Work

5.1 Conclusion

In this thesis, thermal nonlinearity and thermally-induced nonlinearity have been investigated. First, an iterative method has been reported to numerically model the thermal nonlinearity. Second, a numerical method has been adopted to capture the IMD3 in AlN LVRs based on the thermal nonlinear MBVD model. Next, the experimental results of the nonlinear admittance response of both AlN and $LiNbO_3$ resonators at different power level have been compared with the simulations results. The excellent agreement between theory and measurements has confirmed the validity of the analysis on the thermal linearity in LVRs. Finally, the IMD3 in the reflected power of AlN resonators have also been measured at different frequency differences and different power levels respectively. The excellent agreement between theory and measurements has confirmed the analysis on the origin of IMD3 in AlN LVRs. This work has provided a precise theoretical framework to improve the linearity of piezoelectric micro-resonator for commercial RF front end filtering.

5.2 Future Work

Although this thesis provides a good platform for predicting thermal nonlinearities and IMD3 in piezoelectric LVRs, the models can be further improved to more thoroughly describe nonlinearities in LVRs.

5.2.1 Thermal Resistance Based on Finite Element Simulation

Currently, the whole resonator body is assumed to have the same temperature, and only the thermal resistance at the anchors is considered. However, the displacement of the resonator body is not uniform at resonance and thus generates different amounts of heat in different parts of the resonator. To get a more accurate model, a distributed thermal model based on FEM is desirable. By assigning the total power dissipation into different elements according to the displacement amplitude, a thermally-coupled electromechanical simulation is promising for further optimization of the thermal nonlinear model.

5.2.2 Investigation of Other Nonlinearities in LVRs

As discussed in section 2.2, there are other nonlinearities in LVRs, which also affect the resonator performance. These nonlinearities cannot be ignored in certain conditions, especially at ultra-low power levels or high power levels. Study of other nonlinearities will provide deeper insights into further design optimizations and physical limitations for LVRs working in extreme conditions.

5.2.3 Nonlinear Response of RF Systems Based on Piezoelectric LVRs

RF systems, particularly future monolithic filtering front-ends, contain more than one single resonator. It is important to generalize the method discussed in this thesis to the real-world applications. This will be a crucial tool aiding the design of RF systems based on piezoelectric LVRs.

References

[1] H. Fujita, "Microactuators and Micromachines," in *Proceedings of the IEEE,* 1998, vol. 86, no. 8, pp. 1721–1732.

[2] R. T. Howe, R. S. Muller, K. J. Gabriel, and W. S. N. Trimmer, "Silicon micromechanics: sensors and actuators on a chip," *IEEE Spectrum*, vol. 27, no. 7. pp. 29–31, 1990.

[3] K. E. Petersen, "Silicon as a mechanical material," *Proc. IEEE*, vol. 70, no. 5, pp. 420–457, 1982.

[4] H. Lorenz, M. Despont, N. Fahrni, N. LaBianca, P. Renaud, and P. Vettiger, "SU-8: a low-cost negative resist for MEMS," *J. Micromechanics Microengineering*, vol. 7, no. 3, p. 121, 1997.

[5] J. M. Bustillo, R. T. Howe, and R. S. Muller, "Surface micromachining for microelectromechanical systems," *Proc. IEEE*, vol. 86, no. 8, pp. 1552–1574, 1998.

[6] H. Seidel, "The mechanism of anisotropic, electrochemical silicon etching in alkaline solutions," in *Solid-State Sensor and Actuator Workshop, 1990. 4th Technical Digest., IEEE*, 1990, pp. 86–91.

[7] K. A. Cook-Chennault, N. Thambi, and A. M. Sastry, "Powering MEMS portable devices—a review of non-regenerative and regenerative power supply systems with special emphasis on piezoelectric energy harvesting systems," *Smart Mater. Struct.*, vol. 17, no. 4, p. 43001, 2008.

[8] T.-W. Yeow, K. L. E. Law, and A. Goldenberg, "MEMS optical switches," *IEEE Commun. Mag.*, vol. 39, no. 11, pp. 158–163, 2001.

[9] S. P. Pacheco, L. P. B. Katehi, and C.-C. Nguyen, "Design of low actuation voltage RF MEMS switch," in *Microwave Symposium Digest. 2000 IEEE MTT-S International*, 2000, vol. 1, pp. 165–168.

[10] G. Piazza, P. J. Stephanou, and A. P. Al Pisano, "Piezoelectric aluminum nitride vibrating contour-mode MEMS resonators," *J. Microelectromechanical Syst.*, vol. 15, no. 6, pp. 1406–1418, 2006.

[11] P. Zhang, C. Dalton, and G. A. Jullien, "Design and fabrication of MEMS-based microneedle arrays for medical applications," *Microsyst. Technol.*, vol. 15, no. 7, pp. 1073–1082, 2009.

[12] C. Martin-Olmos, H. I. Rasool, B. H. Weiller, and J. K. Gimzewski, "Graphene MEMS: AFM probe performance improvement," *ACS Nano*, vol. 7, no. 5, pp. 4164–4170, 2013.

[13] D. C. Abeysinghe, S. Dasgupta, J. T. Boyd, and H. E. Jackson, "A novel MEMS pressure sensor fabricated on an optical fiber," *IEEE Photonics Technol. Lett.*, vol. 13, no. 9, pp. 993–995, 2001.

[14] J. W. Weigold, T. J. Brosnihan, J. Bergeron, and X. Zhang, "A MEMS condenser microphone for consumer applications," in *19th IEEE International Conference on Micro Electro Mechanical Systems*, 2006, pp. 86–89.

[15] J. Wu, G. K. Fedder, and L. R. Carley, "A low-noise low-offset capacitive sensing amplifier

for a 50-μg/√ Hz monolithic CMOS MEMS accelerometer," *IEEE J. Solid-State Circuits*, vol. 39, no. 5, pp. 722–730, 2004.

[16] H. C. Nathanson, W. E. Newell, R. A. Wickstrom, and J. R. Davis, "The resonant gate transistor," *IEEE Trans. Electron Devices*, vol. 14, no. 3, pp. 117–133, 1967.

[17] G. M. Rebeiz, *RF MEMS: theory, design, and technology*. John Wiley & Sons, 2004.

[18] F. D. Bannon, J. R. Clark, and C.-C. Nguyen, "High-Q HF microelectromechanical filters," *IEEE J. Solid-State Circuits*, vol. 35, no. 4, pp. 512–526, 2000.

[19] R. Ruby, "FBAR — From technology development to production," in *Second International Symposium on Acoustic Wave Devices for Future Mobile Communication Systems*, 2004, p. 5.

[20] H. Chandrahalim, D. Weinstein, L. F. Cheow, S. A. Bhave, and O. Group, "High-κ dielectrically transduced MEMS thickness shear mode resonators and tunable channel-select RF filters," *Sensors Actuators A Phys.*, vol. 136, no. 2, pp. 527–539, 2007.

[21] R. M. C. Mestrom, R. H. B. Fey, J. T. M. Van Beek, K. L. Phan, and H. Nijmeijer, "Modelling the dynamics of a MEMS resonator: simulations and experiments," *Sensors Actuators A Phys.*, vol. 142, no. 1, pp. 306–315, 2008.

[22] M. Rinaldi, C. Zuniga, C. Zuo, and G. Piazza, "AlN contour-mode resonators for narrow-band filters above 3 GHz," in *2009 IEEE International Frequency Control Symposium Joint with the 22nd European Frequency and Time forum*, 2009, pp. 70–74.

[23] R. Ruby, M. Small, F. Bi, D. Lee, L. Callaghan, R. Parker, and S. Ortiz, "Positioning FBAR technology in the frequency and timing domain," *IEEE Trans. Ultrason. Ferroelectr. Freq. Control*, vol. 59, no. 3, pp. 334–345, 2012.

[24] R. E. Pelrine, R. D. Kornbluh, and J. P. Joseph, "Electrostriction of polymer dielectrics with compliant electrodes as a means of actuation," *Sensors Actuators A Phys.*, vol. 64, no. 1, pp. 77–85, 1998.

[25] A. Hajjam, A. Rahafrooz, J. C. Wilson, and S. Pourkamali, "Thermally actuated MEMS resonant sensors for mass measurement of micro/nanoscale aerosol particles," in *Sensors, 2009 IEEE*, 2009, pp. 707–710.

[26] S. Gong and G. Piazza, "Multi-frequency wideband RF filters using high electromechanical coupling laterally vibrating lithium niobate MEMS resonators," *Microelectromechanical Syst. J.* , vol. 23, no. 5, pp. 1188–1197, 2014.

[27] P. Frankovsky, D. Hroncov, I. Delyov, and I. Virgala, "Modeling of dynamic systems in simulation environment MATLAB/Simulink C SimMechanics," *Am. J. Mech. Eng.*, vol. 1, no. 7, pp. 282–288, Dec. 2013.

[28] K. Popp, "Applied structural and mechanical vibrations: theory, methods and measuring instrumentation," *Appl. Mech. Rev.*, vol. 53, no. 8, pp. B77–B77, 2000.

[29] C. Hayashi, *Nonlinear Oscillations in Physical Systems*. Nature Publishing Group, 1986.

[30] V. Kaajakari, T. Mattila, A. Oja, and H. Seppa, "Nonlinear limits for single-crystal silicon microresonators," *J. Microelectromechanical Syst.*, vol. 13, no. 5, pp. 715–724, 2004.

[31] R. Lifshitz and M. C. Cross, "Nonlinear dynamics of nanomechanical resonators,"

Nonlinear Dyn. Nanosyst., pp. 221–266, 2010.

[32] H. K. Khalil and J. W. Grizzle, *Nonlinear Systems*, vol. 3. Prentice Hall, New Jersey, 1996.

[33] C.-M. Lin, T.-T. Yen, V. V Felmetsger, M. A. Hopcroft, J. H. Kuypers, and A. P. Pisano, "Thermally compensated aluminum nitride Lamb wave resonators for high temperature applications," *Appl. Phys. Lett*, vol. 97, no. 8, p. 83501, 2010.

[34] L. G. Villanueva, E. Kenig, R. B. Karabalin, M. H. Matheny, R. Lifshitz, M. C. Cross, and M. L. Roukes, "Surpassing fundamental limits of oscillators using nonlinear resonators," *Phys. Rev. Lett.*, vol. 110, no. 17, pp. 1–5, 2013.

[35] K. Hashimoto, *RF Bulk Acoustic Wave Filters for Communications*. Artech House, 2009.

[36] H. Jaffe and D. A. Berlincourt, "Piezoelectric transducer materials," *Proc. IEEE*, vol. 53, no. 10, pp. 1372–1386, 1965.

[37] J. F. Nye, *Physical Properties of Crystals: Their Representation by Tensors and Matrices*. Oxford University Press, 1985.

[38] G. A. Jeffrey and G. S. Parry, "Crystal structure of aluminum nitride," *J. Chem. Phys.*, vol. 23, no. 2, p. 406, 1955.

[39] H. D. Megaw, "A note on the structure of lithium niobate, LiNbO3," *Acta Crystallogr. Sect. A Cryst. Physics, Diffraction, Theor. Gen. Crystallogr.*, vol. 24, no. 6, pp. 583–588, 1968.

[40] M.-A. Dubois and P. Muralt, "Properties of aluminum nitride thin films for piezoelectric transducers and microwave filter applications," *Appl. Phys. Lett.*, vol. 74, no. 20, pp. 3032–3034, 1999.

[41] Y.-H. Song and S. Gong, "Spurious mode suppression in SH0 lithium niobate laterally vibrating MEMS resonators," in *2015 IEEE International Electron Devices Meeting (IEDM)*, 2015, pp. 15–18.

[42] J. W. Yi, W. Y. Shih, and W.-H. Shih, "Effect of length, width, and mode on the mass detection sensitivity of piezoelectric unimorph cantilevers," *J. Appl. Phys.*, vol. 91, no. 3, pp. 1680–1686, 2002.

[43] C. M. Lin, V. Yantchev, J. Zou, Y. Y. Chen, and A. P. Pisano, "Micromachined one-port aluminum nitride lamb wave resonators utilizing the lowest-order symmetric mode," *J. Microelectromechanical Syst.*, vol. 23, no. 1, pp. 78–91, 2014.

[44] S. Gong and G. Piazza, "Weighted electrode configuration for electromechanical coupling enhancement in a new class of micromachined lithium niobate laterally vibrating resonators," *Tech. Dig. - Int. Electron Devices Meet. IEDM*, pp. 367–370, 2012.

[45] S. Gong and G. Piazza, "Design and analysis of lithium–niobate-based high electromechanical coupling RF-MEMS resonators for wideband filtering," *IEEE Trans. Microw. Theory Tech.*, vol. 61, no. 1, pp. 403–414, 2013.

[46] R. Wang and S. A. Bhave, "Thin-film lithium niobate contour-mode resonators," in *Ultrasonics Symposium (IUS), 2012 IEEE International*, 2012, pp. 303–306.

[47] M. Rinaldi, Y. Hui, C. Zuniga, A. Tazzoli, and G. Piazza, "High frequency AlN MEMS resonators with integrated nano hot plate for temperature controlled operation," in *Frequency Control Symposium (FCS), 2012 IEEE International*, 2012, pp. 1–5.

[48] Y.-H. Song, R. Lu, and S. Gong, "Analysis and removal of spurious response in SH0 lithium niobate MEMS resonators," *IEEE Trans. Electron Devices*, vol. 63, no. 5, pp. 2066–2073, 2016.

[49] M. Rinaldi, C. Zuniga, and G. Piazza, "5-10 GHz AlN contour-mode nanoelectromechanical resonators," in *Micro Electro Mechanical Systems, 2009. MEMS 2009. IEEE 22nd International Conference on*, 2009, pp. 916–919.

[50] V. J. Gokhale, J. Roberts, and M. Rais-Zadeh, "High performance bulk mode gallium nitride resonators and filters," in *2011 16th International Solid-State Sensors, Actuators and Microsystems Conference*, 2011, pp. 926–929.

[51] S. Gong and G. Piazza, "Figure-of-merit enhancement for laterally vibrating lithium niobate mems resonators," *IEEE Trans. Electron Devices*, vol. 60, no. 11, pp. 3888–3894, 2013.

[52] M. Giovannini, S. Yazici, N. K. Kuo, and G. Piazza, "Apodization technique for spurious mode suppression in AlN contour-mode resonators," *Sensors Actuators, A Phys.*, vol. 206, pp. 42–50, 2014.

[53] C. Cassella, J. Segovia-Fernandez, G. Piazza, M. Cremonesi, and a. Frangi, "Reduction of anchor losses by etched slots in aluminum nitride contour mode resonators," *2013 Jt. Eur. Freq. Time Forum Int. Freq. Control Symp. EFTF/IFC 2013*, pp. 926–929, 2013.

[54] S. Gong and G. Piazza, "An 880 MHz ladder filter formed by arrays of laterally vibrating thin film lithium niobate resonators," in *Proceedings of the IEEE International Conference on Micro Electro Mechanical Systems (MEMS)*, 2014, pp. 1241–1244.

[55] C. Zuo, J. Van der Spiegel, and G. Piazza, "1.05-GHz CMOS oscillator based on lateral-field-excited piezoelectric AlN contour-mode MEMS resonators," *IEEE Trans. Ultrason. Ferroelectr. Freq. Control*, vol. 57, no. 1, pp. 82–87, 2010.

[56] S. Ghosh and G. Piazza, "Laterally vibrating resonator based elasto-optic modulation in aluminum nitride," *APL Photonics*, vol. 1, no. 3, p. 36101, 2016.

[57] M. Breen, W. Streyer, R. Lu, A. Gao, D. Wasserman, and S. Gong, "High speed mid-infrared detectors based on MEMS resonators and spectrally selective metamaterials," in *Frequency Control Symposium (IFCS), 2016 IEEE International*, 2016, pp. 1–6.

[58] T. Nan, Y. Hui, M. Rinaldi, and N. X. Sun, "Self-biased 215MHz magnetoelectric NEMS resonator for ultra-sensitive DC magnetic field detection," *Sci. Rep.*, vol. 3, 2013.

[59] T. Manzaneque, J. Hernando, L. Rodríguez-Aragón, A. Ababneh, H. Seidel, U. Schmid, and J. L. Sánchez-Rojas, "Analysis of the quality factor of AlN-actuated micro-resonators in air and liquid," *Microsyst. Technol.*, vol. 16, no. 5, pp. 837–845, 2010.

[60] J. Segovia-Fernandez and G. Piazza, "Thermal nonlinearities in contour mode AlN resonators," *J. Microelectromechanical Syst.*, vol. 22, no. 4, pp. 976–985, 2013.

[61] S. Gong and G. Piazza, "Multi-frequency wideband RF filters using high electromechanical coupling laterally vibrating lithium niobate MEMS resonators," *Proc. IEEE Int. Conf. Micro Electro Mech. Syst.*, pp. 785–788, 2013.

[62] D. A. Feld and D. S. Shim, "Determination of the nonlinear physical constants in a piezoelectric AlN film," in *Ultrasonics Symposium (IUS), 2010 IEEE*, 2010, pp. 277–282.

[63] W. Sahyoun, J.-M. Duchamp, and P. Benech, “Acoustic, piezoelectric, and dielectric nonlinearities of AlN in coupled resonator filters for high RF power levels,” *IEEE Trans. Ultrason. Ferroelectr. Freq. Control*, vol. 58, no. 10, pp. 2162–2170, 2011.

[64] K. M. Lakin, K. T. McCarron, and J. F. McDonald, “Temperature compensated bulk acoustic thin film resonators,” in *Ultrasonics Symposium, 2000 IEEE*, 2000, vol. 1, pp. 855–858.

[65] R. B. Karabalin, X. L. Feng, and M. L. Roukes, “Parametric nanomechanical amplification at very high frequency,” *Nano Lett.*, vol. 9, pp. 3116–3123, 2009.

[66] R. Lu, A. Gao, and S. Gong, “Parametric excitation in geometrically optimized AlN contour mode resonators,” in *Frequency Control and the European Frequency and Time Forum (FCS), 2015 Joint Conference of the IEEE International*, 2015, no. April 2015, pp. 15–18.

[67] P. Mejzl’ik, “A bisection method to find all solutions of a system of nonlinear equations,” in *Domain Decomposition Methods in Scientific and Engineering Computing: Proceedings of the Seventh International Conference on Domain Decomposition*, 1994, vol. 180, pp. 277–282.

[68] D. M. Pozar, *Microwave Engineering*. John Wiley & Sons, 2009.

[69] E. Rocas, C. Collado, J. Mateu, H. Campanella, and J. M. O’Callaghan, “Third order intermodulation distortion in film bulk acoustic resonators at resonance and antiresonance,” in *Microwave Symposium Digest, 2008 IEEE MTT-S International*, 2008, pp. 1259–1262.

[70] C. D. Nordquist and R. H. Olsson, “Power handling and intermodulation distortion of contour-mode AlN MEMS resonators and filters,” in *Microwave Symposium Digest (MTT), 2011 IEEE MTT-S International*, 2011, pp. 1–4.

[71] A. Gao and S. Gong, “Eradication of asymmetric spurious mode in AlN MEMS resonators using mode conversion of Lamb waves,” in *IEEE 29th International Conference on Micro Electro Mechanical Systems (MEMS)*, 2016.

[72] J. Segovia-Fernandez, M. Cremonesi, C. Cassella, A. Frangi, and G. Piazza, “Anchor losses in AlN contour mode resonators,” *J. Microelectromechanical Syst.*, vol. 24, no. 2, pp. 265–275, Apr. 2015.

[73] S. Gong and G. Piazza, “Design and analysis of lithium-niobate-based high electromechanical coupling RF-MEMS resonators for wideband filtering,” *IEEE Trans. Microw. Theory Tech.*, vol. 61, no. 1, pp. 403–414, 2013.

[74] F. W. Sears, M. W. Zemansky, and H. D. Young, *University Physics*. Addison-Wesley, 1987.

[75] S. R. Choi, D. Kim, S.-H. Choa, S.-H. Lee, and J.-K. Kim, “Thermal conductivity of AlN and SiC thin films,” *Int. J. Thermophys.*, vol. 27, no. 3, pp. 896–905, Sep. 2006.

[76] R. S. Weis and T. K. Gaylord, “Lithium niobate: summary of physical properties and crystal structure,” *Appl. Phys. A*, vol. 37, no. 4, pp. 191–203, 1985.

Appendix Code

A.1 Code for Thermal Nonlinearity Model

```
ClearAll["Global`*"]
ws = ws0 (1 + TCF * T);
Rm = π * π / 8 * 1 / (C0 * kt * kt * Q * ws);
Lm = π * π / 8 * 1 / (C0 * kt * kt * ws * ws);
Cm = 8 / π / π * C0 * kt * kt;
Rm0 = π * π / 8 * 1 / (C0 * kt * kt * Q * ws0);
Cm0 = 8 / π / π * C0 * kt * kt;
Lm0 = π * π / 8 * 1 / (C0 * kt * kt * ws0 * ws0);

Z = FullSimplify[1 / (j * w * C0 + 1 / (Rm + j * w * Lm + 1 / (j * w * Cm)))]
ReZ = FullSimplify[ComplexExpand[Re[Z]]]
lista = Join[Range[2 * π *1015 * 10^6, 2 * π * 1027 * 10^6, 2 * π * 0.05 * 10^6]];
(*lista={272.992*10^6*2*π};*)
output = {};
outputT = {};
Tsave = 0;
Do[{
  Clear[T, T2, w];
  Q = 100;
  kt = Sqrt[0.077]; C0 = 173.1774 * 10^-15; ws0 = 2 * π * 1022 * 10^6; TCF = -30 * 10^-6;
  Rth = 35; Cth = 10.4 * 10^-8;
  w = wf;
  P = 29;
  P1 = (10^(P / 10 - 3));
  ZS = 141.25;
  n = 1;
  Voc = 2 * Sqrt[ZS * P1];
  m = 0;
  T2 = Tsave;
  firstflag = 1;
  Yout = 0; flag = 1;
  (*Tmin=0;*)Tmin = ReleaseHold[Tsave]; Tmax = 1000;
  While[True, {
    Clear[T];
    T = ReleaseHold[T2];
```

```
m++;
    (*sol=NDSolve[{(Abs[V/Z])^2*ReZ-2*x[t]/Rth==Cth*D[x[t],{t,1}],x[0]== 0},{x[t]},
      {t,0,0.02},MaxSteps->Infinity];
    T2=NMaximize[{x[t]/.sol[[1]],0.009<t<0.01},t][[1]];*)
    T2 = (Abs[Voc / (Z + ZS)])^2 * ReZ * Rth / n;
    If[firstflag == 1, {If[T2 < T, {Clear[T]; (*Print["!"];*)
          Tsave = 0;
          Tmin = 0;
          Tmax = ReleaseHold[T];
          T = 0;
          m++;
          T2 = (Abs[Voc / (Z + ZS)])^2 * ReZ * Rth / n;
          T2 = 0.9;
          (*sol=NDSolve[{(Abs[V/Z])^2*ReZ-2*x[t]/Rth==Cth*D[x[t],{t,1}],x[0]== 0},
            {x[t]},{t,0,0.02},MaxSteps->Infinity];
          T2=NMaximize[{x[t]/.sol[[1]],0.009<t<0.01},t][[1]];*)}, Tmin = ReleaseHold[T];];
       firstflag = 0;}];
    (*Print["??",T,"??",T2];*)
    If[Abs[T - T2] < 0.0001, {Yout = 20 * Log10[Abs[1 / Z]];
       output = Append[output, {wf, Yout}]; outputT = Append[outputT, {wf, T2}];
       (*Print["frequency ",wf/2/π,"done, T ",T,", loop number ",m];*)Break[]}];
    If[m > 2000, {(*T2=(T+T2)/2;Clear[T];
       T=T2;Yout=20*Log10[Abs[1/Z]];
       output=Append[output,{wf,Yout}];*)
       Print[wf / 2 / π, "not done, T ", T, ", T2 ", T2]; Break[]}];
    (*Print[T,",",T2];*)
    If[(flag == 1 && T2 > T) || (flag == 0 && T2 < T), {T2 = ReleaseHold[(T + T2) / 2];
       flag = flag;},
      {T2 = ReleaseHold[0.5 * Sort[{T2, Tmin, T, Tmax}][[2]] + 0.5 * Sort[{T2, Tmin, T, Tmax}][[3]]];
       flag = 1 - flag;
       If[flag == 1, Tmax = ReleaseHold[T], Tmin = ReleaseHold[T]];
      }];
    Tsave = ReleaseHold[T];
    (*Print[T2,",",m,",",flag];*)}]
  }, {wf, lista}]
a = ListLinePlot[output, PlotStyle → Blue]
b = Plot[20 * Log10[Abs[1 / Z]], {w, 2 * π *1015 * 10^6, 2 * π * 1025 * 10^6}, PlotRange → All,
  PlotStyle → Green]
Show[a, b]
c = ListLinePlot[outputT, PlotStyle → Blue, PlotRange → All]
```

A.2 Code for Intermodulation Model

```
close all;
clear all;
clc;
Pa =5;
Pb =5;
deltafreq=1000;
```

```
mkdir(num2str(deltafreq));
samp_freq=1e9;
tspan = 0:1/(samp_freq):0.09;
options = odeset('MaxStep', 1e-5);
% [T Y] = ode23(@diff_lu, [0 0.1],0, options);
[T Y] = ode23(@diff_lu_t, tspan,0, options);
fig1=figure('visible','off');
plot(T,Y);
saveas(fig1, strcat(num2str(deltafreq),'/figure1.png'));
temp=size(T);
length=temp(1)/9*8;
X = fft(Y(size(Y)/21:size(Y)))*2/length;
timelength=0.08
X(1)=X(1)/2;
fig2=figure('visible','off');
% plot((0:99)/timelength,abs(X(1:100)));
plot((0:deltafreq/2)/timelength,abs(X(1:deltafreq/2+1)));
saveas(fig2, strcat(num2str(deltafreq),'/figure2.png'));
kt=sqrt(0.0163);
C0=460*10^-15;
ws0=456.4*10^6*2*3.1415926;
TCF=-30*10^-6;
Rth=3500;
Cth=30*10^-8;
Q=987*1.01;
deltaw=2*pi*deltafreq;
ws=ws0*(1+TCF*Y);
Rm=pi*pi/8*1./(C0*kt*kt*Q.*ws);
Lm=pi*pi/8*1./(C0*kt*kt*ws.*ws);
Cm=8/pi/pi*C0*kt*kt;
w1=ws0-deltaw;
w2=ws0+deltaw;
Z1=1./(i*w1*C0+1./(Rm+i*w1*Lm+1./(i*w1*Cm)));
Z2=1./(i*w2*C0+1./(Rm+i*w2*Lm+1./(i*w2*Cm)));
ReZ1=real(Z1);
ReZ2=real(Z2);
P1 = (10^(Pa/10 - 3));
P2 = (10^(Pb/10 - 3));
Voc1=2*sqrt(50*P1);
Voc2=2*sqrt(50*P2);
Vback =
real(Voc1.*exp(i*w1*T).*50./(2*50+Z1)+Vdevice2.*exp(i*w2*T).*50./(2*50+
Z2));
fig3=figure('visible','off');
plot(T,Vback);
saveas(fig3, strcat(num2str(deltafreq),'/figure3.png'));
X2 = fft(Vback(size(Vback)/9:size(Vback)))*2/length;
X2(1)=X2(1)/2;
% figure;
% plot((0:99)/0.07,abs(X2(1:100)));
fig4=figure('visible','off');
lowlim=timelength*ws0/2/pi+1-10*deltafreq*timelength;
highlim=timelength*ws0/2/pi+1+10*deltafreq*timelength;
frange=linspace(ws0/2/pi-10*deltafreq,ws0/2/pi+10*deltafreq,1-
round(lowlim)+round(highlim));
plot(frange,abs(X2(round(lowlim):round(highlim))));
saveas(fig4, strcat(num2str(deltafreq),'/figure4.png'));
```

```
plot(frange,10*log10(1000*abs(X2(round(lowlim):round(highlim)).*X2(roun
d(lowlim):round(highlim))/50)));
saveas(fig5, strcat(num2str(deltafreq),'/figure5.png'));
index=[round(timelength*ws0/2/pi+1-
3*deltafreq*timelength),round(timelength*ws0/2/pi+1-
1*deltafreq*timelength),round(timelength*ws0/2/pi+1+1*deltafreq*timelen
gth),round(timelength*ws0/2/pi+1+3*deltafreq*timelength)]
save=10*log10(1000*abs(X2(index).*X2(index)/50))
dlmwrite(strcat(num2str(deltafreq),'/RT.txt'),save,'\t')
save2=10*log10(1000*abs(X2(round(lowlim):round(highlim)).*X2(round(lowl
im):round(highlim))/50));
dlmwrite(strcat(num2str(deltafreq),'/RT2.txt'),save2,'\t');

function [dy] = diff_lu_t(t, y)
    deltafreq=1000;
    kt=sqrt(0.0163);
    C0=460*10^-15;
    ws0=456.4*10^6*2*3.1415926;
    TCF=-30*10^-6;
    Rth=3500;
    Cth=30*10^-8;
    Q=987*1.01;
    ws=ws0*(1+TCF*y);
    Rm=pi*pi/8*1/(C0*kt*kt*Q*ws);
    Lm=pi*pi/8*1/(C0*kt*kt*ws*ws);
    Cm=8/pi/pi*C0*kt*kt;
    deltaw=2*pi*deltafreq;
    w1=ws0-deltaw;
    w2=ws0+deltaw;
    w0=ws0;
    Z1=1./(i*w1*C0+1./(Rm+i*w1*Lm+1./(i*w1*Cm)));
    Z2=1./(i*w2*C0+1./(Rm+i*w2*Lm+1./(i*w2*Cm)));
    Z0=1./(i*w0*C0+1./(Rm+i*w0*Lm+1./(i*w0*Cm)));
    ReZ1=real(Z1);
    ReZ2=real(Z2);
    ReZ0=real(Z0);

    Pa =5;
    Pb =5;
    P1 = (10^(Pa/10 - 3));
    P2 = (10^(Pb/10 - 3));
    Voc1=2*sqrt(50*P1);
    Vdevice1=Voc1.*((Z1)./(Z1 + 2*50));
    Voc2=2*sqrt(50*P2);
    Vdevice2=Voc2.*((Z2)./(Z2 + 2*50));
    flag=(Vdevice1>Vdevice2);
    dy =-y/Cth/Rth+1/Cth*ReZ1*(abs((Vdevice1-
Vdevce2)*flag/Z1))^2+1/Cth*ReZ2*(abs((Vdevice2-Vdevice1)*(1-
flag)/Z2))^2+1/Cth*ReZ0*(abs((Vdevice2*flag+Vdevice1*(1-
flag))*2*cos(deltaw*t)/Z0))^2;
end
```